Meteoritics & Planetary Science 35, 1333–1354 (2000)

A petrographic, chemical, and isotopic study of calcium-aluminum-rich inclusions and aluminum-rich chondrules from the Axtell (CV3) chondrite

G. SRINIVASAN†, G. R. HUSS‡* AND G. J. WASSERBURG

Division of Geological and Planetary Sciences, Mail Code 170-25, California Institute of Technology, Pasadena, California 91125, USA
†Present address: Physical Research Laboratory, Navrangpura, Ahmedabad 380009, India
‡Present address: Department of Geology and Center for Meteorite Studies, Arizona State University, P.O. Box 871404, Tempe, Arizona 85297-1404, USA
*Correspondence author's e-mail address: gary.huss@asu.edu

(Received 1999 November 17; accepted in revised form 2000 August 7)

Abstract–Petrographic, compositional, and isotopic characteristics were studied for three calcium-aluminum-rich inclusions (CAIs) and four plagioclase-bearing chondrules (three of them Al-rich) from the Axtell (CV3) chondrite. All seven objects have analogues in Allende (CV3) and other primitive chondrites, yet Axtell, like most other chondrites, contains a distinctive suite of CAIs and chondrules. In common with Allende CAIs, CAIs in Axtell exhibit initial $^{26}Al/^{27}Al$ ratios ($(^{26}Al/^{27}Al)_0$) ranging from $\sim 5 \times 10^{-5}$ to $< 1.1 \times 10^{-5}$, and plagioclase-bearing chondrules have $(^{26}Al/^{27}Al)_0$ ratios of $\sim 3 \times 10^{-6}$ and lower. One type-A CAI has the characteristics of a FUN inclusion. The Al-Mg data imply that the plagioclase-bearing chondrules began to form >2 Ma after the first CAIs. As in other CV3 chondrites, some objects in Axtell show evidence of isotopic disturbance. Axtell has experienced only mild thermal metamorphism (<600 °C), probably not enough to disturb the Al-Mg systematics. Its CAIs and chondrules have suffered extensive metasomatism, probably prior to final accretion. These data indicate that CAIs and chondrules in Axtell (and other meteorites) had an extended history of several million years before their incorporation into the Axtell parent body. These long time periods appear to require a mechanism in the early solar system to prevent CAIs and chondrules from falling into the Sun *via* gas drag for several million years before final accretion.

We also examined the compositional relationships among the four plagioclase-bearing chondrules (two with large anorthite laths and two barred-olivine chondrules) and between the chondrules and CAIs. Three processes were examined: (1) igneous differentiation, (2) assimilation of a CAI by average nebular material, and (3) evaporation of volatile elements from average nebular material. We find no evidence that igneous differentiation played a role in producing the chondrule compositions, although the barred olivine compositions can be related by addition or subtraction of olivine. Methods (2) and (3) could have produced the composition of one chondrule, AXCH-1471, but neither process explains the other compositions. Our study indicates that plagioclase-bearing objects originated through a variety of processes.

INTRODUCTION

We report on an integrated study of the petrology, chemical composition, and isotopic systematics (Al-Mg and Ti) of calcium-aluminum-rich inclusions (CAIs) and plagioclase-bearing chondrules in the Axtell (CV3) chondrite. Axtell has been described by Simon *et al.* (1995), who consider it to have experienced less secondary metamorphism than Allende (CV3) based on a wider distribution of fayalite contents of matrix olivines, lower thermoluminescence (TL) sensitivity, and lower degree of sulfidization in Axtell. The existing Al-Mg database for CV3 meteorites is dominated by Allende (Lee *et al.*, 1976, 1977, 1979; cf., review by MacPherson *et al.*, 1995). Other CV3 chondrites for which significant amounts of Al-Mg data are available include Leoville (Stegmann and Begemann, 1981; Caillet *et al.*, 1993); Vigarano (Hutcheon *et al.*, 1986; MacPherson and Davis, 1993; Loss *et al.*, 1994), and Efremovka (Fahey *et al.*, 1987a; Goswami *et al.*, 1994). A few data are available for Grosnaja and Kaba (Hutcheon *et al.*, 1986), Ningqiang and Acfer 082 (MacPherson *et al.*, 1995). We studied Axtell to (1) extend the information about the ^{26}Al-^{26}Mg system to another CV meteorite and (2) investigate a suite of CAIs and plagioclase-rich chondrules from a single meteorite apparently less altered than Allende to unravel the relative contributions of formation conditions and metamorphism. The only previous isotopic study on Axtell was by Caillet and Zinner (1995) of a hercynite-rich inclusion with large ^{48}Ca and ^{50}Ti excesses, but no evidence of ^{26}Al.

The broader problem relating to ^{26}Al in meteorites can be summarized as follows: (1) many CAIs formed with initial $^{26}Al/^{27}Al$ ratios ($(^{26}Al/^{27}Al)_0$) of $\sim 5 \times 10^{-5}$, both in CV3 chondrites and in other meteorite classes (review by MacPherson *et al.*, 1995; Russell *et al.*, 1996; Guan *et al.*, 2000); (2) some CAIs show $(^{26}Al/^{27}Al)_0 << 5 \times 10^{-5}$ (*e.g.*, Lee *et al.*, 1979); (3) some plagioclase-bearing and glass-rich chondrules in CV3 chondrites and unequilibrated ordinary chondrites show evidence of $(^{26}Al/^{27}Al)_0 \approx (0.3–1) \times 10^{-5}$, but many show no evidence of ^{26}Al (Sheng *et al.*, 1991; Russell *et al.*, 1996; Moustefauoi *et al.*, 1999; McKeegan *et al.*, 2000); and (4) a few CAIs exhibit deficits in $^{26}Mg/^{24}Mg$ that cannot be readily explained in terms of ^{26}Al (Wasserburg and Papanastassiou, 1982; Ireland *et al.*, 1991; Russell *et al.*, 1998). Interpretation of these observations is critical to our understanding of early solar system processes. With regard to CAIs and chondrules in Axtell, it is necessary to consider metamorphism both on the immediate Axtell parent body and during the history of the objects prior to accretion of the parent body.

Preliminary reports of this work were presented by Srinivasan *et al.* (1996, 1997).

EXPERIMENTAL TECHNIQUE

Fourteen thin sections prepared from two pieces of a ~200 g slice of Axtell were studied by optical and scanning electron microscope. Three CAIs (two type A and one type B (Grossman, 1975)) and four plagioclase-bearing chondrules were selected for

detailed petrographic, compositional, and isotopic studies. Labels (*e.g.*, AXCAI-2771) consist of meteorite initials, "CAI" or "CH" (chondrule), piece number, section number, and number of the object in the thin section. The seven objects were mapped with backscattered electron (BSE) images, minerals were identified, and modal abundances were estimated by point counting the BSE maps. Major and minor element compositions of minerals were determined with the Caltech JEOL 733 electron microprobe. Bulk compositions of CAIs and chondrules were estimated from mineral compositions and modes converted to weight percent.

Trace element abundances were determined with PANURGE, a modified Cameca ims-3f ion microprobe, following standard procedures (Zinner and Crozaz, 1986; Fahey *et al.*, 1987b). Secondary ions were measured at low mass-resolving power with 80 eV of energy filtering to suppress the signals of complex molecular interferences. Signals for rare earth elements (REE) were deconvolved from REE-monoxide signals using linear algebra (Zinner and Crozaz, 1986). Ion signals were normalized to the Ca signal for all minerals, except olivine, where Si was the reference element. Calcium and Si contents were determined by electron probe. Sensitivity factors were determined from a synthetic Ti-pyroxene glass, NBS 610 and 612 glasses, Madagascar hibonite, Alnö (Sweden) perovskite, and Angra Dos Reis pyroxene. Reported uncertainties (2σ) are from counting statistics and do not include the 5–10% uncertainties inherent in the abundance calibrations.

Magnesium isotopes were measured using standard techniques (Huneke *et al.*, 1983; Fahey *et al.*, 1987a,b). Carbon-coated thin sections were bombarded with a focused $^{16}O^-$ primary ion beam energized to 17 keV. Primary beam currents of 0.2–0.7 nA gave beam diameters of ≤ 5 μm. The $^{24}Mg^+$ count rate was kept below 2×10^5 counts/sec to minimize deadtime corrections. A mass resolving power of ~3000 was used to resolve $^{25}Mg^+$ from $^{24}MgH^+$. The intrinsic isotopic mass fractionation for the sample minerals (F_{Mg}) was found by comparing the measured $^{25}Mg/^{24}Mg$ ratios for the samples with the ratios measured in the appropriate terrestrial mineral standards (Burma spinel, melilite glass, Madagascar hibonite, San Carlos olivine, and natural diopside) and is given by

$$F_{Mg} = (\Delta^{25}Mg)_{sample} - (\Delta^{25}Mg)_{standard} \text{ (‰/amu)} \quad (1)$$

where $\Delta^i Mg = (((^iMg/^{24}Mg)_{measured}/(^iMg/^{24}Mg)_{reference}) - 1) \times 1000$. The reference value used for $^{25}Mg/^{24}Mg$ was 0.12663 (Catanzarro *et al.*, 1966). The reference value for $^{26}Mg/^{24}Mg$ determined from analyses of terrestrial standards is 0.13955 (Brigham, 1990). Shifts in $^{26}Mg/^{24}Mg$ ($\delta^{26}Mg$) were calculated using a linear mass fractionation law and are reported as

$$\delta^{26}Mg = \Delta^{26}Mg - (2 \times \Delta^{25}Mg) \quad \text{(‰/amu)} \quad (2)$$

The $^{27}Al/^{24}Mg$ values for each mineral were corrected for differential ionization efficiency using sensitivity factors determined from appropriate mineral standards.

Titanium isotopes were measured in perovskite from one CAI at a mass-resolving power of ~7500 following procedures of Fahey *et al.* (1987a,b) and Ireland *et al.* (1991). Standards were Madagascar hibonite and San Benito perovskite. Interferences from ^{50}V and ^{50}Cr at ^{50}Ti were monitored by measuring ^{51}V and ^{52}Cr and ranged in perovskite from $<<0.1$‰ for ^{50}V to 0.5–1.5‰ for ^{50}Cr. The interference from ^{46}Ca on ^{46}Ti (~3.5‰) was monitored by measuring ^{44}Ca, and the interference from $^{88}Sr^{2+}$ at ^{44}Ca was monitored at mass 43.5 ($^{87}Sr^{2+}$). A correction was made for the tail of ^{48}Ca on ^{48}Ti, but for perovskite the correction was ≤ 0.3‰. To correct for instrumental mass fractionation, a fractionation factor, α, was calculated from $^{46}Ti/^{48}Ti$ according to the "exponential" mass fractionation law (Russell *et al.*, 1978):

$$\frac{(^{46}Ti/^{48}Ti)_{meas}}{(^{46}Ti/^{48}Ti)_{std}} = \left(\frac{m_{46}}{m_{48}}\right)^{\alpha} \quad (3)$$

The calculated "α" was then used to correct the remaining ratios according to

$$\left(\frac{^iTi}{^{48}Ti}\right)_{corr} = \left(\frac{^iTi}{^{48}Ti}\right)_{meas} \times \left(\frac{m_i}{m_{48}}\right)^{-\alpha} \quad (4)$$

Terrestrial isotope ratios were taken from Niederer *et al.* (1981). Intrinsic mass fractionation, obtained by comparing the measured isotope ratios with those measured on the appropriate terrestrial standard, is reported as F_{Ti} in permil per amu (‰/amu) relative to the terrestrial compositions. Isotopic anomalies remaining after accounting for mass fractionation are reported in permil relative to terrestrial values:

$$\delta^i Ti = \left(\frac{(^iTi/^{48}Ti)_{corr}}{(^iTi/^{48}Ti)_{terr}} - 1\right) \times 1000 \quad (5)$$

All isotopic data are reported with $2\sigma_{mean}$ uncertainties.

PETROGRAPHY AND MINERAL CHEMISTRY

Axtell is an oxidized CV3 chondrite with a general appearance similar to the oxidized CV3, Allende. However, Axtell escaped the strong sulfidization experienced by Allende and has experienced a slightly lower grade of thermal metamorphism (Simon *et al.*, 1995). Although Axtell is a find, the degree of terrestrial weathering is low and weathering has not affected the chondrules and CAIs. Detailed descriptions of three CAIs and four chondrules are given below. Modal mineral abundances are presented in Table 1, and example and average mineral compositions are given in Tables 2 and 3.

Calcium-Aluminum-Rich Inclusions

One large (2 × 3 mm) compact type-A CAI appears in three thin sections. The three pieces are labeled AXCAI-2271, AXCAI-2771, and AXCAI-2571 (Fig. 1a,b,c). Henceforth, the inclusion will be referred to as AXCAI-2771 (after the piece with the largest area). Inclusion AXCAI-2771 consists primarily of melilite and spinel, with minor perovskite and hibonite (Table 1). It is irregular in shape and its surface is deeply embayed. A particularly deep embayment was exposed resulting in an "inclusion" of matrix (Fig. 1b). A thin (30–50 μm) rim sequence similar to rims found on Allende CAIs (Wark and Lovering, 1977) surrounds the entire inclusion, including inside the large embayment (Fig. 1b). Secondary mineralization occurs inside the rim and along cracks penetrating the interior (Fig. 1).

Melilite in AXCAI-2771 forms lath-shaped crystals up to 1 mm long. Most of the melilite is relatively Mg-rich (~$Åk_{20-36}$), and the crystals are not regularly zoned. Melilite within ~50 μm of the surface of the inclusion is much more gehlenitic (~$Åk_{8-10}$) (Table 2). Over much of the inclusion, particularly in section 2271, the melilite contains high concentrations of 5–20 μm spinel crystals (Fig. 1a,b).

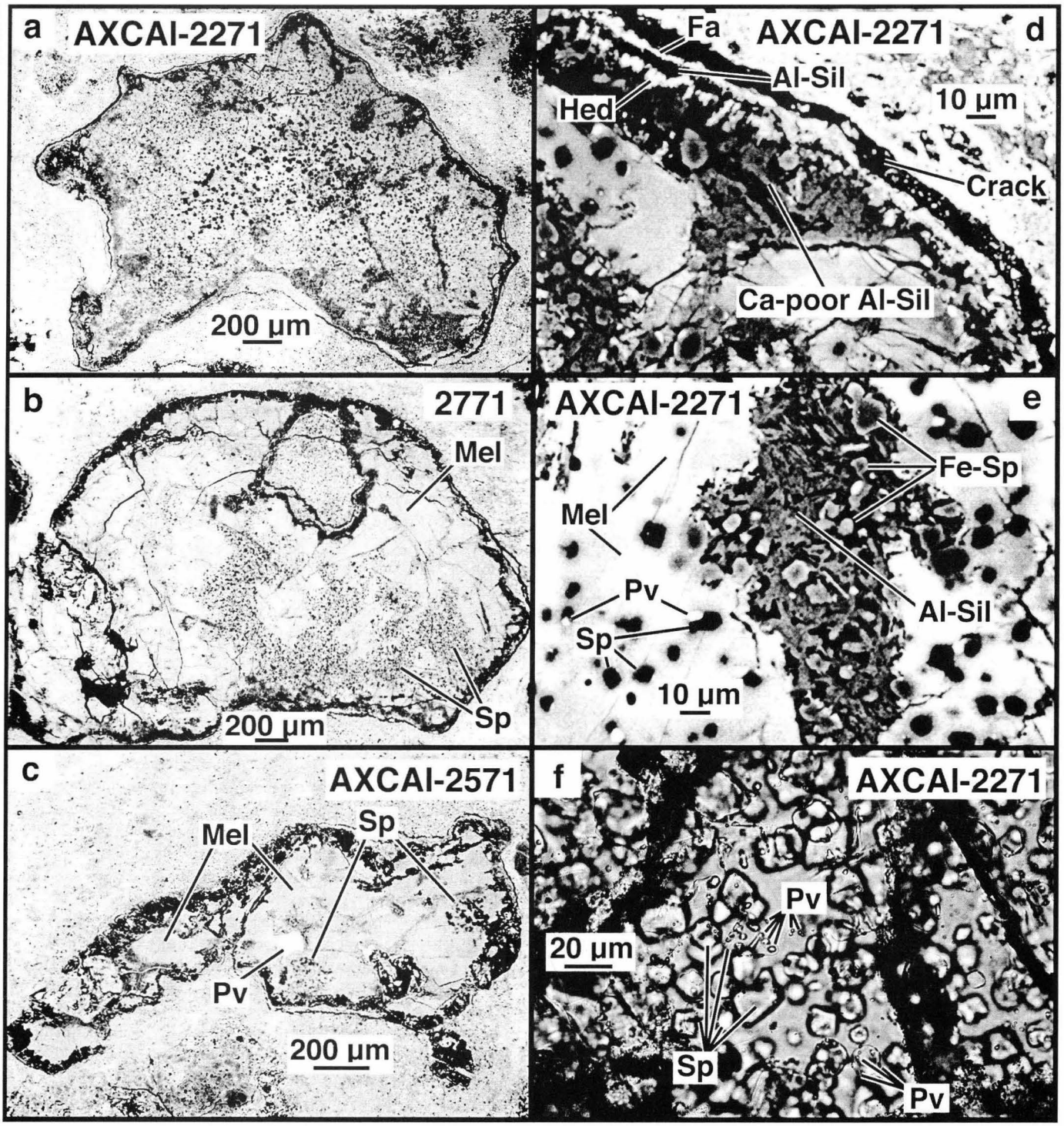

FIG. 1. AXCAI-2771: Panels (a), (b), and (c) show backscattered electron (BSE) images of three sections of this large compact type-A CAI. (c) Section AXCAI-2571 consists almost entirely of melilite (Mel) with a few inclusions of spinel (Sp) and perovskite (Pv). The other two sections are also dominantly melilite, but with higher concentrations of spinel. (d) High-magnification BSE image of the rim sequence, which consists of a discontinuous thin outer layer of fayalite (Fa) overlying a thin layer of aluminosilicate (Al-Sil) overlying a thin layer of hedenbergite (Hed), all of which overly a thicker layer of Fe-rich, Ca-poor aluminosilicate (Ca-poor Al-Sil). (e) High-magnification BSE image of the alteration that occurs at the margins of the inclusion and along cracks. Secondary aluminosilicate appears to have formed from melilite through Ca loss and Fe gain. Spinel in the altered regions is Fe-rich, with higher FeO contents at the grain surfaces (lighter color = higher FeO content). Perovskite often occurs in contact with spinel. (f) Transmitted light image of spinel grains in melilite. Many of the spinel grains have rounded shapes and only a few show distinct crystal faces. The surfaces of both rounded and euhedral spinels are decorated with tiny crystals of perovskite.

TABLE 1. Modal abundances of major mineral phases in Axtell CAIs and chondrules (vol%).

	AXCAI-2771	AXCAI-1571	AXCAI-2775	AXCH-1471	AXCH-1371	AXCH-2171	AXCH-2272
Melilite	85.7 ± 3.3*	66.6 ± 4.6*	45.0 ± 5.6	–	–	–	–
Anorthite	–	–	5.0 ± 1.9	46.4 ± 5.0	56.7 ± 5.7	38.8 ± 5.2†	5.9 ± 1.2†
Pyroxene	–	–	35.0 ± 4.9	35.7 ± 4.4	40.3 ± 4.8	22.1 ± 3.9†	5.5 ± 1.1†
Olivine	–	–	–	13.9 ± 2.7	2.5 ± 1.2	39.1 ± 5.2	79.5 ± 4.4
Spinel	13.0 ± 1.3	11.3 ± 1.9	15.0 ± 3.2	4.0 ± 1.5	0.6 ± 0.6	–	–
Perovskite	1.0 ± 0.4	2.1 ± 0.8	–	–	–	–	–
Hibonite	0.3 ± 0.2	0.9 ± 0.5	–	–	–	–	–
Mesostasis	–	–	–	–	–	–	7.4 ± 1.3‡
Metal	–	–	–	–	–	–	1.7 ± 0.6
Rim spinel	–	15.9 ± 2.2	–	–	–	–	–
Rim silicate	–	3.2 ± 1.0	–	–	–	–	–

*Melilite abundance calculated assuming that alteration phases were originally melilite.
†Anorthite and pyroxene make up the mesostasis between the olivine grains.
‡"Mesostasis" in AXCH-2272 refers to finely intergrown plagioclase and pyroxene in roughly equal proportions.

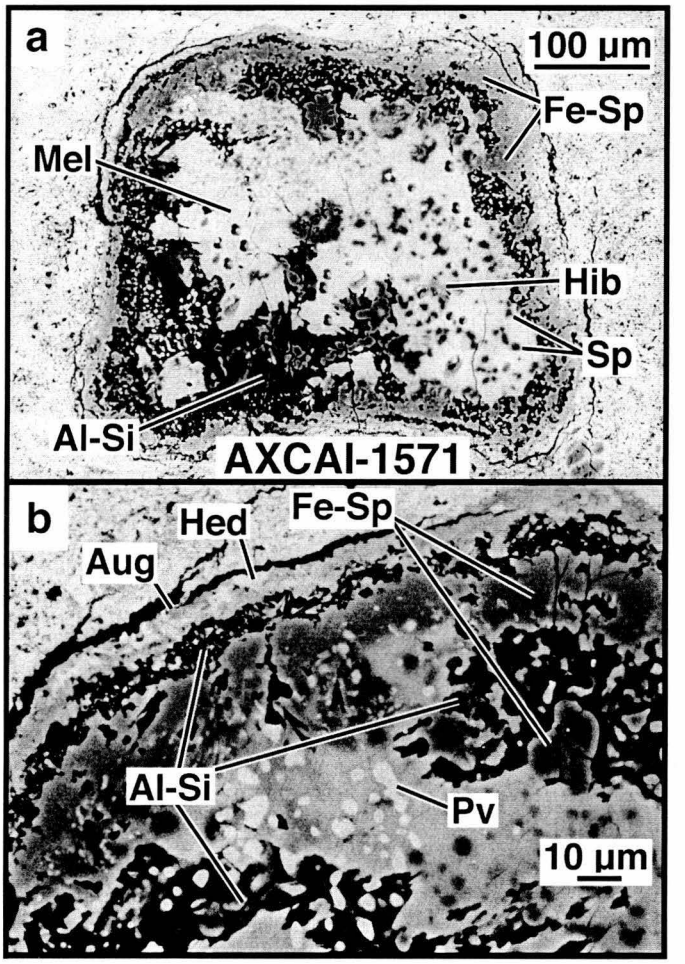

FIG. 2. Backscattered electron images of AXCAI-1571, a compact type-A CAI composed of melilite (Mel) enclosing Mg-Al spinel (Sp), hibonite (Hib), and perovskite (Pv). A well-developed rim sequence (b) consists of Fe-rich spinel, overlain by a discontinuous layer of aluminosilicate, followed in turn by a continuous outer layer of intergrown hedenbergite (Hed) and ferroan augite (Aug). Secondary aluminosilicate (Al-Si) occurs within ~50 μm of the rim and penetrates the interior along cracks. Spinel within the altered regions is Fe-rich.

Spinel is much less abundant in section 2571 (Fig. 1c). A few spinel grains have euhedral outlines, but most are rounded, which suggests that they are partially resorbed (Fig. 1f). Spinel in unaltered regions is essentially pure $MgAl_2O_4$, with minor Cr, V, and Ti (Table 2). Spinel grains are decorated with numerous tiny crystals of pervoskite (Fig. 1e,f). Perovskite grains in spinel-rich regions range up to ~20 μm. In spinel-poor regions, perovskite grains tend to be fewer and larger (up to ~100 μm), apparently because there were few spinel grains to help the perovskite nucleate. Perovskite has traces of Al, Si, and V (Table 2). A few 20–40 μm hibonite laths with moderate TiO_2 and MgO (Table 2) are present near the margins of the inclusion.

The rim surrounding AXCAI-2771 consists of four distinct layers. Outermost is a discontinuous thin layer of fayalitic olivine (Fa_{40-80}), which overlies a thin layer of aluminosilicate. Inside of these layers is a continuous 5–10 μm thick layer of pyroxene (ranging from hedenbergite to almost augite) with occasional hibonite laths. Inside the pyroxene layer is a 10–40 μm thick layer of aluminosilicate (Al/Si = 0.5–1.75) containing Na, Cl, K, Ca, and Fe. This layer appears to have formed by metasomatism of melilite. Inside the rim and along cracks penetrating the interior, melilite has been altered to secondary minerals similar to those observed in Allende CAIs (Fig. 1). Heavily altered regions consist of Ca-poor, Fe-rich aluminosilicate containing varying amounts of Mg, Na, Cl, and K, whereas lightly altered areas consist of a mixture of 2–5 μm laths of melilite surrounded by aluminosilicate with less Ca than melilite (Fig. 1e). Spinel in the altered regions is Fe-rich (Table 2).

Inclusion AXCAI-1571 is a ~400 μm compact type-A CAI (Fig. 2). It consists primarily of 40–100 μm elongate melilite crystals enclosing 10–30 μm spinel grains, 2–5 μm perovskites, and a few 5–10 μm hibonite crystals (Table 1). Spinel and perovskite are somewhat more abundant near the edges of the inclusion. Hibonite occurs in contact with spinel, which may have served as a nucleation site for hibonite. Melilite compositions cover the range ~$Åk_{8-26}$ (Table 2), but most crystals are ~$Åk_{20}$ and the inclusion does not show radial zoning. Spinels have rounded shapes and in unaltered areas are almost pure $MgAl_2O_4$, but with relatively high V_2O_3 contents. Hibonite in AXCAI-1571 is richer in TiO_2 and V_2O_3 and has less FeO than that in AXCAI-2771 (Table 2). The inclusion has a well-developed rim sequence consisting of a 10–30 μm layer of Fe-rich spinel overlain by a discontinuous layer of porous,

TABLE 2. Mineral compositions of Axtell CAIs (wt%).

AXCAI-2771 (Type A)

	Melilite				Spinel		Perovskite	Hibonite
	Int. #1	Int. #2	Edge	Average	Fe-poor	Fe-rich*	Average	Average
SiO_2	29.78	26.17	23.48	26.53	0.07	0.03	0.10	0.16
TiO_2	0.06	0.08	0.14	0.07	0.66	0.22	56.64	4.87
Al_2O_3	23.51	29.36	33.41	28.53	70.08	65.26	0.26	82.10
Cr_2O_3	0.03	0.00	0.01	0.01	0.45	0.08	0.02	0.09
FeO	0.00	0.00	0.02	0.03	0.07	11.23	0.01	0.15
MnO	0.00	0.00	0.00	0.01	0.01	0.00	0.04	0.01
MgO	5.18	2.91	1.25	3.19	27.96	20.32	0.00	3.02
CaO	40.94	41.34	40.98	40.94	0.12	0.16	41.09	8.16
Na_2O	0.08	0.00	0.03	0.02	0.00	0.00	0.00	0.00
K_2O	0.04	0.02	0.01	0.02	0.01	0.00	0.02	0.00
V_2O_3	0.04	0.03	0.01	0.01	0.42	0.40	0.12	0.24
NiO	0.12	0.08	0.02	0.06	0.03	0.01	0.03	0.02
Total	99.78	99.99	99.36	99.42	99.88	97.71	98.33	98.82
	AK_{36}	AK_{20}	AK_9	$n = 39$	$n = 8$	$n = 1$	$n = 2$	$n = 4$

AXCAI-1571 (Type A)

	Melilite			Spinel		Perovskite	Hibonite
	#1	#2	Average	Interior	Rim		Average
SiO_2	26.95	24.03	25.86	0.04	0.03	0.13	0.23
TiO_2	0.03	0.00	0.04	0.18	0.20	55.29	6.79
Al_2O_3	28.18	32.70	30.18	69.92	68.38	0.47	80.06
Cr_2O_3	0.03	0.02	0.01	0.11	0.15	0.03	0.02
FeO	0.07	0.00	0.04	0.13	7.05	0.00	0.05
MnO	0.01	0.00	0.01	nm	nm	0.00	0.02
MgO	3.30	1.46	2.55	28.31	23.69	0.02	3.70
CaO	40.50	39.90	40.18	0.11	0.07	39.83	8.43
Na_2O	0.01	0.10	0.05	nm	nm	0.00	0.00
K_2O	0.01	0.02	0.02	nm	nm	0.03	0.00
V_2O_3	0.00	0.00	0.01	0.82	0.38	0.48	0.47
NiO	0.00	0.02	0.02	nm	nm	0.00	0.04
Total	99.09	98.25	98.97	99.62	99.95	96.28	99.81
	AK_{23}	AK_{10}	$n = 8$	$n = 4$	$n = 1$	–	$n = 2$

AXCAI-2775 (Type B)

	Melilite			Pyroxene (Fassaite)			Anorthite	Spinel
	Edge	Interior	Average	#1	#2	Average	Average	Average
SiO_2	27.33	25.14	26.24	31.63	33.81	33.10	42.95	0.13
TiO_2	0.06	0.03	0.03	13.06	10.55	11.91	0.02	0.30
Al_2O_3	28.36	31.05	29.55	23.89	23.11	22.66	36.44	70.56
Cr_2O_3	0.00	0.02	0.02	0.08	0.07	0.07	0.04	0.19
FeO	0.17	0.03	0.10	0.02	0.09	0.06	0.07	0.55
MnO	0.01	0.00	0.02	0.03	0.03	0.01	0.02	0.01
MgO	3.27	2.23	3.01	5.65	7.01	6.58	0.02	27.54
CaO	40.10	41.19	40.47	25.02	24.96	24.95	20.28	0.33
Na_2O	0.17	0.08	0.11	0.02	0.01	0.01	0.06	0.00
K_2O	0.02	0.01	0.02	0.01	0.02	0.02	0.03	0.01
V_2O_3	0.06	0.01	0.02	0.26	0.15	0.18	0.01	0.13
NiO	0.27	0.05	0.24	0.00	0.12	0.04	0.07	0.02
Total	99.82	99.84	99.81	99.67	99.93	99.59	100.01	99.77
	AK_{23}	AK_{15}	$n = 6$	–	–	$n = 5$	$n = 2$	$n = 3$

*In altered region. nm = not measured.

poorly crystallized aluminosilicate with minor Ca, Mg, Fe, and Cr followed by an outer layer consisting of a fine-grained intergrowth of hedenbergite and ferroan augite (Fig. 2b). The two outer layers also contain minor spinel and pervoskite. Rim spinels are more Fe-rich in the outer layers, with FeO > 50 mol% in the pyroxene zone. However, spinel just inside the thick layer of Fe-rich-spinel is Fe-free. About 25% of the melilite in the inclusion, particularly that just inside the spinel rim and along cracks penetrating the interior, has been replaced by poorly crystallized, porous aluminosilicate (Fig. 2b). This material has an Al/Si ratio of ~0.5, low but variable amounts of Ca, and traces of Fe. Spinel grains in the recrystallized regions have Fe-rich rims.

Inclusion AXCAI-2775 is an oval, 1.2 × 1.0 mm, type-B2 CAI. Primary phases are melilite, fassaite, anorthite, spinel, and perovskite (Table 1). Melilite occurs as large, often lath-shaped crystals up to 400 μm in length. These crystals are polygranular and their structure is consistent with metamophic recrystallization. Melilite shows some compositional variability ($Åk_{15-23}$), but no regular zoning. Fassaite occurs as equant, anhedral crystals up to ~100 μm and exhibits moderate compositional variability. The TiO_2 content of fassaite (10–13%) is at the upper end of the range exhibited by Allende type-B inclusions. Fassaite in most Allende type-B inclusions has 3–11% TiO_2, although a few inclusions have pyroxene with 16–18% TiO_2 (Grossman, 1975; Wark and Lovering, 1982). Plagioclase is present as small subhedral to anhedral crystals up to ~50 μm and is essentially pure anorthite (Table 2). Since anorthite typically crystallizes from Mg-rich melts with a few tenths of percent MgO (cf., Table 3), the very low concentration of Mg in this anorthite from AXCAI-2775 may reflect mild metamorphism. Spinel grains occur as 2–10 μm crystals, typically with rounded shapes. Spinel grains are found in melilite or fassite, but not in anorthite and occasionally form 20–50 μm clusters. Perovskite occurs primarily as tiny 1–2 μm blebs. The inclusion has an exterior 30–50 μm rim of augitic to hedenbergitic pyroxene, with the most Fe-rich material on the outer surface. Inside the pyroxene layer is a layer of porous aluminosilicate containing Ca, Na, K, and Fe. Iron-rich spinel occurs in the outer portions of this altered layer, but spinel in the unaltered melilite just inside this zone is Fe-free.

Plagioclase-Bearing Chondrules

Chondrule AXCH-1471 is a large (~2.8 mm), spherical chondrule that appears in three adjacent thin sections (AXCH-1471, AXCH-1372, and AXCH-1671). Thin section AXCH-1471, a near equatorial slice, gives the object its name. This chondrule is dominated by large twinned anorthite laths ranging up to 100 × 1500 μm in size (Fig. 3). In AXCH-1671, a section from near the chondrule surface, a cluster of large plagioclase laths radiate from a single point. Plagioclase crystals are clean and show no signs of alteration. Pyroxene is the main interstitial phase. Within and between anorthite and pyroxene crystals, and unevenly distributed, are 50–400 μm suhedral to anhedral olivine grains. Numerous 5–10 μm spinel grains occur most commonly in anorthite and occasionally form round palisade structures ~125 μm in diameter (Fig. 3b). Around much of the outer portion of the chondrule, smaller pyroxene laths with interstitial anorthite dominate (Fig. 3b). The outer region is essentially free of olivine and spinel.

Anorthite (An_{95-97}) has relatively high concentrations of Fe and Mg (Table 3), which is consistent with a low degree of metamorphism. Pyroxene is aluminous diopside with 2.0–2.5% TiO_2. Pyroxene in the finer-grained, spinel-poor region tends to have lower Al_2O_3 and higher MgO contents than the large interior crystals. Olivine (Fo_{98}) has a relatively high CaO content. Most spinels have approximately 1–2% FeO and Cr_2O_3 and are unzoned except for thin Fe-rich rims. These FeO and Cr_2O_3 contents are higher than those in CAI spinels (cf., Table 2 and 3). Many spinels are rounded and appear somewhat resorbed. A few spinels have FeO ≈ 5–7% and irregular, rounded

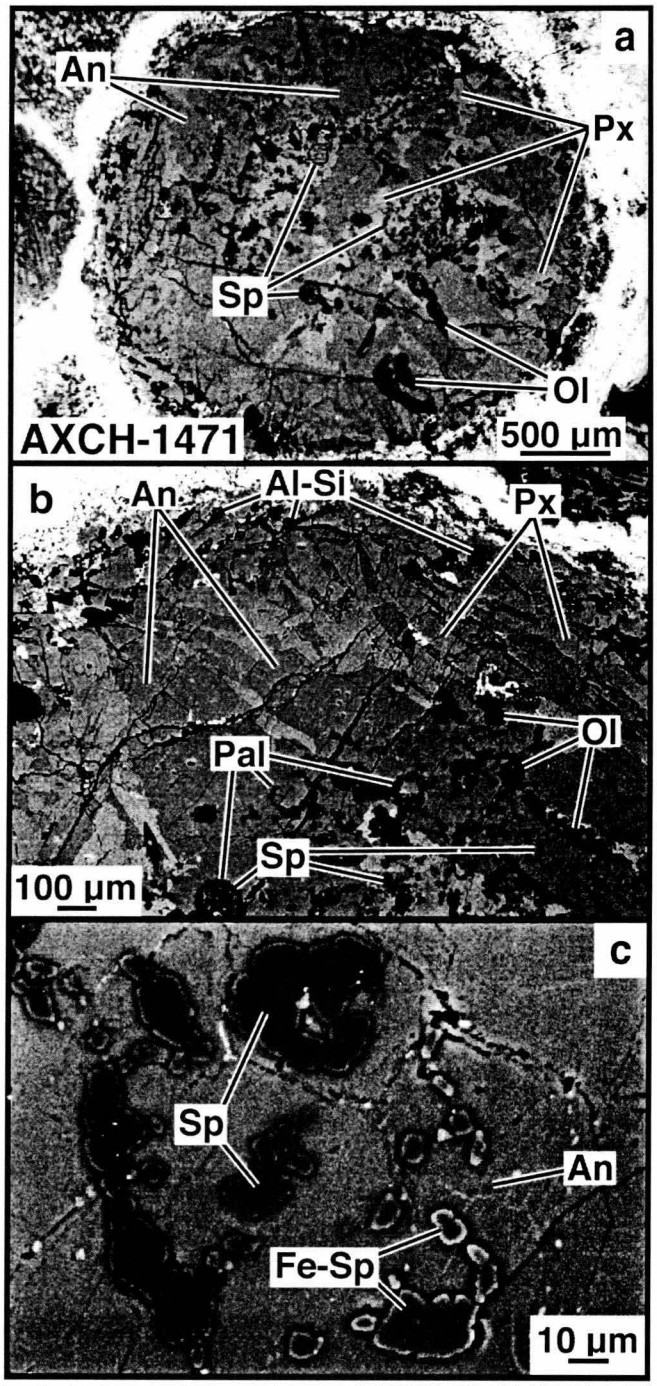

FIG. 3. Backscattered electron images of AXCH-1471. (a) This chondrule consists of large anorthite laths (An) and interstitial pyroxene (Px) enclosing subhedral olivine crystals (Ol) and spinel grains (Sp). (b) View of the chondrule margin showing radiating pyroxene laths with interstitial anorthite. Secondary aluminosilicate (Al-Si) replaces anorthite near the chondrule surface. (c) Two types of spinel are observed. Most spinel is euhedral to subhedral and Mg-rich (Sp) and occasionally forms palisade bodies (Pal). Some spinel is Fe-rich (Fe-Sp) and consists of rounded crystals (partially resorbed?) whose rims have very high Fe contents.

TABLE 3. Mineral compositions of Axtell chondrules (wt%).

AXCH-1471

	Pyroxene		Anorthite	Olivine	Normal	Resorbed Spinel	
	Edge	Interior	An_{95-97}	Fo_{98}	Spinel	Core	Rim
SiO_2	49.04	46.80	43.51	41.94	0.23	0.09	0.17
TiO_2	2.17	2.51	0.04	0.07	0.32	0.31	0.31
Al_2O_3	7.73	9.85	35.18	0.20	69.42	68.41	67.25
Cr_2O_3	0.63	0.45	0.01	0.16	1.03	0.79	1.36
FeO	0.29	0.20	0.22	1.80	1.82	5.64	6.80
MnO	0.04	0.03	0.01	0.07	0.02	0.00	0.00
MgO	15.86	14.30	0.38	54.41	27.38	24.64	23.78
CaO	23.15	24.38	19.34	0.69	0.16	0.13	0.20
Na_2O	0.02	0.01	0.41	0.01	0.00	0.00	0.00
K_2O	0.02	0.02	0.02	0.02	0.01	0.01	0.02
V_2O_3	0.13	0.14	0.01	0.02	0.37	0.43	0.41
NiO	0.01	0.01	0.01	0.04	0.01	0.03	0.04
Total	99.09	98.70	99.14	99.43	100.77	100.48	100.34
	$n=3$	$n=4$	$n=7$	$n=3$	$n=4$	–	–

AXCH-1371

	Pyroxene		Anorthite	Olivine	Spinel
	Edge	Interior	An_{97-98}	Fo_{98-100}	
SiO_2	48.04	47.82	42.99	42.05	0.43
TiO_2	0.69	2.03	0.03	0.09	0.33
Al_2O_3	10.66	9.99	35.69	0.16	67.66
Cr_2O_3	0.35	0.35	0.01	0.19	0.91
FeO	0.24	0.17	0.22	1.16	5.62
MnO	0.03	0.02	0.01	0.06	0.05
MgO	14.18	14.95	0.20	55.17	24.14
CaO	23.89	23.84	19.65	0.78	0.28
Na_2O	0.00	0.01	0.28	0.00	0.00
K_2O	0.01	0.02	0.03	0.02	0.00
V_2O_3	0.02	0.11	0.01	0.06	0.13
NiO	0.04	0.02	0.03	0.02	0.00
Total	98.15	99.33	99.15	99.76	99.55
	$n=1$	$n=6$	$n=7$	$n=3$	–

	AXCH-2171			AXCH-2272		
	Olivine Fo_{99}	Plagioclase An_{90-96}	Pyroxene	Olivine Fo_{98}	Plagioclase An_{85}	Pyroxene
SiO_2	41.71	43.69	56.86	40.56	44.79	58.92
TiO_2	0.16	0.04	0.91	0.08	0.05	0.63
Al_2O_3	0.32	34.43	2.34	0.22	32.79	2.08
Cr_2O_3	0.37	0.02	0.80	0.27	0.01	0.54
FeO	1.24	0.17	0.76	2.15	0.50	0.41
MnO	0.11	0.02	0.22	0.05	0.01	0.03
MgO	54.56	0.44	33.16	55.05	0.65	33.07
CaO	0.37	19.20	5.54	0.19	17.59	5.53
Na_2O	0.03	0.68	0.02	0.03	1.69	0.05
K_2O	0.03	0.02	0.01	0.02	0.02	0.06
V_2O_3	0.07	0.01	0.02	0.01	0.00	0.00
NiO	0.07	0.04	0.04	0.05	0.00	0.01
Total	99.04	98.76	100.68	98.68	98.11	101.33
	$n=3$	$n=7$	$n=6$	$n=6$	$n=3$	$n=4$

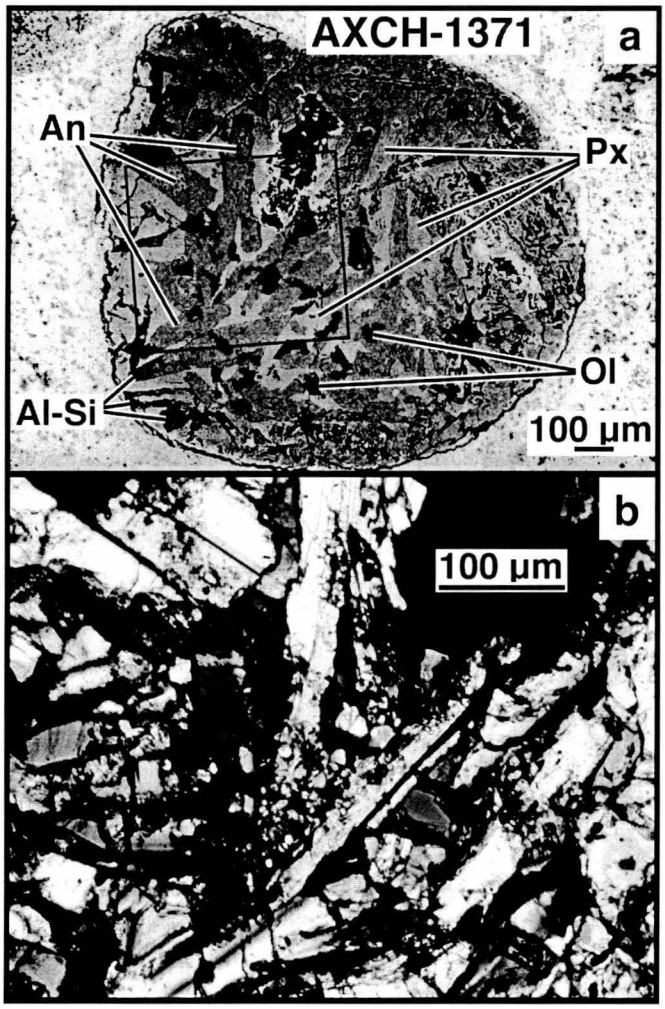

FIG. 4. Backscattered electron (a) and reflected light (b) images of AXCH-1371. Two distinct regions are visible. In the coarse-grained region, large anorthite laths (An) and interstitial pyroxene (Px) enclose smaller crystals of olivine (Ol). In the fine-grained region (bottom and right margins in (a)), laths of pyroxene, which appear to have nucleated on the surface of the chondrule, extend inward with interstitial anorthite. Near the edge of the chondrule, anorthite has been partially replaced by aluminosilicate (Al-Si), some of which was plucked during sectioning.

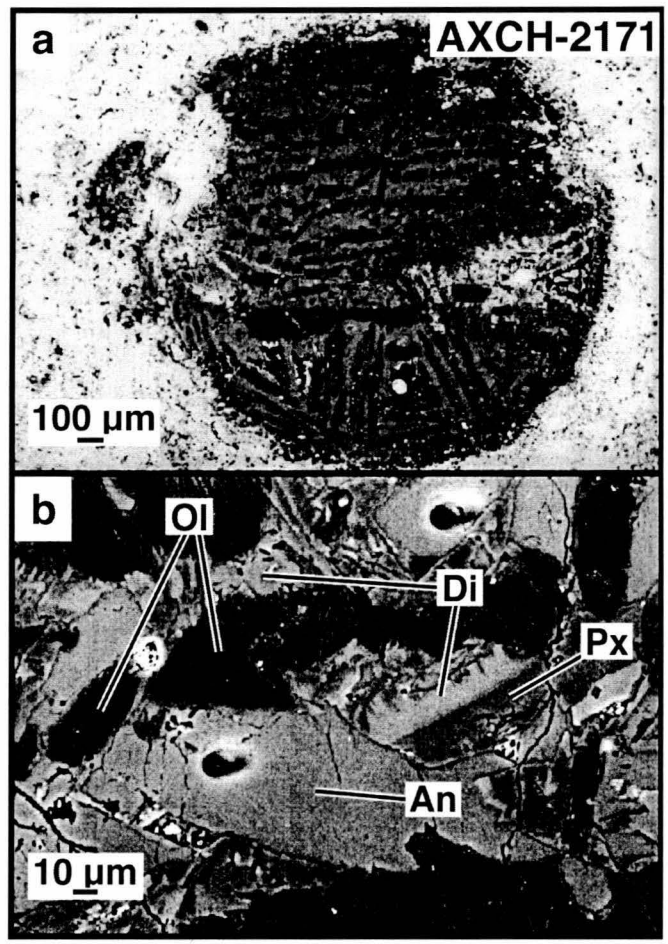

FIG. 5. Backscattered electron images of the barred-olivine chondrule, AXCH-2171. (a) Multiple sets of olivine bars enclose a mesostasis of anorthite and pyroxene. In heavily altered regions (top right and on the left and right sides), olivine laths have been broken into equant fragments with FeO-rich edges, and mesostasis has been leached, leaving a porous material composed of Si, Al, Mg, Ca, Fe, and Ni. (b) High-magnification view of the mesostasis, which consists of anorthite, a Ca-rich pyroxene with compositions approaching diopside (Di), and a low-Ca, high Mg pyroxene (Px). The intimate relationship of the two pyroxenes suggests exsolution from an original pigeonite. Two ion probe spots are visible in the anorthite (top right, center left).

shapes (Fig. 3c). The FeO contents of these spinels increases toward their rims and they may be partially resorbed relic grains. In a zone ~100 μm wide around the edge of the chondrule, anorthite has been partially replaced by porous aluminosilicate. A few small hedenbergite crystals occur along cracks. Olivine crystals are slightly more Fe-rich at their surfaces and along cracks, indicating secondary introduction of Fe. There is no convincing evidence of a rim.

Chondrule AXCH-1371 is a ~1.3 mm chondrule with a protrusion on one end (Fig. 4) composed of plagioclase, aluminous diopside, and olivine (Table 1). Tiny spinel grains (1–5 μm) are found primarily within the anorthite crystals (Fig. 4b), and troilite blebs (5–20 μm) occur in widely spaced clusters. Chondrule AXCH-1371 exhibits two discrete textural regions (Fig. 4). In the main portion, anorthite occurs as subhedral to euhedral laths ranging in size from approximately 20 × 100 μm to approximately 50 × 700 μm with pyroxene as the main interstitial phase. Anorthite and pyroxene occasionally enclose subhedral 20–100 μm olivine crystals. Around two-thirds of the perimeter, there is a 100–300 μm layer of pyroxene laths with smaller, interstitial plagioclase laths. Olivine is absent in this region. Over the remaining one-third of the perimeter, the large anorthite and pyroxene crystals of the main portion are truncated by the chondrule surface. Plagioclase (An_{97-98}) has relatively high FeO and MgO contents. Aluminous diopside has a higher TiO_2 content in the coarse-grained interior than in the finer-grained outer region. Olivine (Fo_{98-100}) has a high CaO content. Most spinel grains are too small to give reliable compositions, but one larger spinel is relatively Fe-rich. In the outer finer-grained region, some of the plagioclase has been replaced by a mixture of fayalitic olivine and a porous aluminosilicate like that in CAIs. In some places, the chondrule is coated by a 5–8 μm rim of fayalitic olivine (~Fa_{40}). This olivine has essentially the same composition as the matrix and as the secondary olivine within the chondrule. Chondrule AXCH-1371 has the texture and mineralogy of a microgabbro. It may be either an abraded melt-drop chondrule or a partially melted lithic fragment that was abraded.

Chondrule AXCH-2171 is a barred olivine chondrule ~1.8 mm in diameter (Fig. 5a). Olivine occurs as sets of bars up to 700 μm long and in a 30 μm layer at the chondrule surface. Interstitial

material consists of plagioclase and pyroxene crystals several tens of micrometers in length (Fig. 5b). Olivine was originally very forsteritic (~Fo_{99}), and the plagioclase between the olivine bars was originally ~An_{96} (Table 3). Two pyroxenes occur in the interstitial material. One is apparently diopside, but the grains are too small to get a good composition. The other is a low-Ca, high-Mg pyroxene. These pyroxenes apparently formed *via* exsolution of an original pigeonite. About 25% of the chondrule has been extensively altered (Fig. 5a). Olivine bars have been fractured perpendicular to their length into equant fragments. These fragments range from ~Fo_{96} at their centers to Fo_{20-40} on the edges. Interstitial anorthite and pyroxene have been replaced with a porous material made up of oxides of Si, Al, Mg, Ca, Fe, and Ni in varying proportions. In these regions, surviving anorthite is more sodic (~An_{90}). Small patches of aluminosilicate similar to that observed in Axtell CAIs are also present between the olivine bars. Highly altered regions contain small grains of hedenbergite. The original surface of the chondrule has been partially abraded and is currently coated with a layer of fine-grained laths of fayalitic olivine (~Fo_{20-40}), similar to matrix olivines. Olivines in the surface layer are more Fe-rich at their rims.

Chondrule AXCH-2272 is a barred olivine chondrule (Fig. 6a). A 100–150 μm layer of olivine appears to define the original dimensions of the chondrule (~1 mm in diameter). The interior consists of three distinct sets of olivine bars that intersect at ~60° angles (Fig. 6a). The interstitial material consists of a mixture of plagioclase and pyroxene. Again, some areas have experienced secondary alteration. Most of the olivine is ~Fo_{98} but is more Fe-rich at the edges of the olivine grains and along cracks. Tiny spherical inclusions of magnetite (probably originally Fe-Ni metal or troilite) are enclosed in the olivines. Interstitial plagioclase (~An_{85}) is more sodic than in AXCH-2171. Two pyroxenes are present, one diopsidic and the other a MgO-rich, CaO-poor pyroxene (Fig. 6b). We only obtained analyses of CaO-poor pyroxene (Table 3). Limited areas of the interstitial material have been leached and partially replaced by secondary minerals. Outside the thick olivine layer is another layer of forsterite, which is FeO-rich at the edges and along cracks. Patches of porous aluminosilicate, fayalite, and minor augite and hedenbergite are regularly dispersed throughout this outer layer.

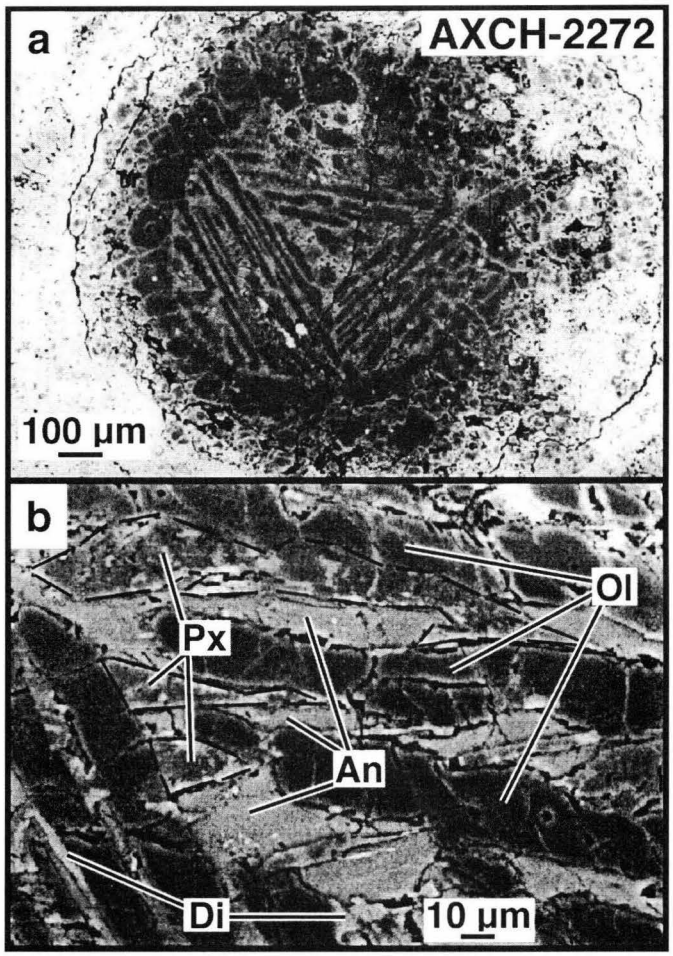

FIG. 6. Backscattered electron images of the barred-olivine chondrule, AXCH-2272. (a) Olivine forms a 100–150 μm layer around the outside of the chondrule and three discrete sets of bars. The chondrule has areas of alteration where mesostasis has been leached and replaced with FeO-rich material (top center and at the bottom just left of center). A poorly defined layer of forsterite with FeO-rich rims, fayalite, aluminosilicate, and minor augite and hedenbergite occurs outside of the thick forsterite layer. (b) High-magnification view of the mesostasis. Between the olivine bars (Ol) is an assemblage of anorthite (An) and two pyroxenes, one Ca-rich (Di) and one Ca-poor and Mg-rich (Px). These pyroxenes are intimately intergrown and appear to have exsolved from an original pigeonite (*e.g.*, outlined areas).

BULK COMPOSITIONS OF CALCIUM-ALUMINUM-RICH INCLUSIONS AND PLAGIOCLASE-BEARING CHONDRULES

Bulk Major and Minor Element Compositions

Calcium-Aluminum-rich Inclusions–Bulk compositions were determined from modal abundances (Table 1) and average mineral compositions (Table 2). Alteration products were not included in the calculation and their volumes were assigned to the inferred original minerals. The calculated compositions are compared to compositions of CAIs from other CV3 meteorites in Table 4. Inclusion AXCAI-2771 and the interior portion of AXCAI-1571 have bulk compositions very similar to compact type-A inclusions from Allende (Table 4). Both Axtell and Allende inclusions differ somewhat from the Leoville compact type-A inclusion, LEO-3536-2, and from the Allende fluffy type-A inclusion, CG-11. The type-B2 inclusion, AXCAI-2775, is similar to type-B inclusions from Allende, Leoville, and Vigarano, except that AXCAI-2775 has a significantly higher TiO_2 content and its Al_2O_3 content falls at the upper end of the range exhibited by Allende inclusions (Table 4; Mason and Martin, 1977; Mason and Taylor, 1982). Allende inclusions often have higher FeO and Na_2O contents than Axtell CAIs (Table 4). This difference may in part reflect the fact that alteration products were not included by us when determining the bulk compositions of Axtell inclusions. Much of the literature data consists of measurements of macroscopic samples of CAIs, and Allende inclusions which often contain nepheline, sodalite, grossular, sulfides, and other secondary phases (*e.g.*, Hutcheon *et al.*, 1978; MacPherson *et al.*, 1988). However, Axtell has significantly lower Na_2O and S contents than Allende (Table 5), so it may be that Axtell inclusions are less altered than those in Allende.

Plagioclase-Bearing Chondrules–Bulk compositions of Axtell plagioclase-bearing chondrules, calculated using data in Tables 1 and 3, are given in Table 6 together with compositions for chondrules from other meteorites. Three of the Axtell chondrules are Al-rich (Al_2O_3 > 10%), whereas AXCH-2272 has a composition similar to type-IA ferromagnesian chondrules (Table 6). Although Al-rich chondrules have a wide range in compositions, they have several features in common. They have much higher TiO_2, Al_2O_3,

TABLE 4. Bulk compositions of Axtell CAIs and similar inclusions from other meteorites.

	Melilite-rich									
	AXCAI-2771	AXCAI-1571		Allende						LEO 3536-2#
Type	CTA	with Rim	w/o Rim CTA	TS-2* CTA	TS-12* CTA	TS-32* CTA	3898†	3529-45‡	CG-11§ FTA	CTA
SiO_2	22.1	17.6	20.5	26.1	22.1	28.0	24.9	26.3	25.1	31.2
TiO_2	0.90	1.65	2.07	0.72	0.59	0.96	1.4	1.4	1.0	1.6
Al_2O_3	34.6	41.0	36.2	29.0	35.8	25.8	32.6	34.3	37.6	23.1
Cr_2O_3	0.08	0.05	0.03	nm	nm	nm	nm	nm	0.02	0.01
FeO	0.04	2.15	0.05	nd	nd	nd	0.88	1.8	1.7	0.54
MnO	0.01	0.01	0.01	nm	nm	nm	nm	nm	0.01	0.02
MgO	6.9	9.8	6.6	10.3	6.0	5.7	6.9	4.1	4.3	5.4
CaO	34.7	26.7	33.3	33.9	35.5	39.5	33.3	32.0	29.4	37.9
Na_2O	0.02	0.04	0.04	nm	nm	nm	0.18	0.07	0.8	0.11
K_2O	0.02	0.01	0.02	nm	nm	nm	<0.01	nm	nm	nm
V_2O_3	0.07	0.20	0.16	nm	nm	nm	nm	nm	0.09	0.06
NiO	0.05	0.01	0.02	nm	nm	nm	nm	nm	0.03	0.04
Totals	99.49	99.22	99.00	100.02	99.99	99.96	100.16	99.97	100.05	99.98

	Type B								
	AXCAI-2775	Allende					LEO 3537-1#	Vigarano	
Type	B2	TS-23* B1	TS-33* B1	3529-45‡	3682‡	3529-G§ B1	3529-Z‡	B2	1623-8$ B2	477-b$ B1
SiO_2	25.1	28.9	27.1	26.3	29.6	29.8	30.9	25.7	24.0	19.4
TiO_2	4.4	1.3	2.8	1.4	1.4	0.99	1.2	1.5	1.9	2.6
Al_2O_3	34.2	28.4	32.9	34.3	27.7	31.6	28.9	34.9	33.1	37.3
Cr_2O_3	0.07	nm	nm	nm	nm	nm	nm	0.06	0.06	0.08
FeO	0.16	0.03	0.01	1.8	4.1	0.37	0.30	0.45	0.57	0.53
MnO	0.02	nm	nm	nm	nm	nm	nm	<0.001	0.002	0.001
MgO	8.3	8.6	7.7	4.1	10.7	10.8	9.3	13.7	12.4	16.8
CaO	27.2	32.9	29.8	32.0	26.3	26.8	29.4	23.4	27.5	22.9
Na_2O	0.05	nm	nm	0.07	0.22	0.11	0.18	0.05	0.08	0.06
K_2O	0.02	nm	nm	nm	nm	<0.01	nm	nm	0.005	0.007
V_2O_3	0.09	nm	nm	nm	nm	nm	nm	0.20	0.11	0.18
NiO	0.12	nm	nm	nm	nm	nm	nm	0.09	0.26	0.13
Totals	99.73	100.13	100.31	99.97	100.02	100.47	100.18	100.05	99.99	99.99

*Beckett (1986).
†Mason and Martin (1977).
‡Mason and Taylor (1982).
§Davis *et al.* (1978).
#Mao *et al.* (1990), SiO_2 by difference.
$Sylvester *et al.* (1992), SiO_2 by difference.
Abbreviations: CTA = compact type-A, FTA = fluffy type-A, LEO = Leoville, nm = not measured, nd = not detected.

and CaO contents and lower MgO contents than ferromagnesian chondrules (Table 6). The high Na_2O contents of Allende plagioclase-olivine inclusions (POIs) probably reflect secondary metasomatism (cf., Sheng *et al.*, 1991). We excluded secondary phases when estimating the compositions of Axtell chondrules. Aluminum-rich chondrules have CaO and Al_2O_3 contents intermediate between those of CAIs (Table 4) and ferromagnesian chondrules (Table 6; Jones and Scott, 1989). However, the relationships between these three classes of objects are not clear (Russell *et al.*, 1996; MacPherson and Huss, 2000). We return to this issue later in Origin of Aluminum-Rich Chondrules.

Trace Element Abundances

Calcium-Aluminum-Rich Inclusions–Figure 7 shows trace element and REE abundances for three Axtell CAIs and their constituent minerals normalized to abundances in CI chondrites. Perovskite is the major host phase for REEs in type-A inclusions. In AXCAI-2771, perovskite has a nearly flat light (L)REE pattern and increasingly depleted heavy (H)REEs. Superimposed on this general pattern are a large negative Eu anomaly and positive anomalies in Tm and Yb (Fig. 7a). Melilite has a similar pattern but with a small positive Eu anomaly. The bulk inclusion has a muted Group II pattern (Mason and Martin, 1977). In AXCAI-1571, perovskite, melilite, and hibonite have patterns similar to those in AXCAI-2771, except that perovskite and hibonite have no Eu anomaly and melilite has a large positive Eu anomaly (Fig. 7b). The bulk pattern for AXCAI-1571 also resembles a muted Group II pattern except for the positive Eu anomaly. In the type-A inclusions, the perovskite-melilite partition coefficient for REEs is ~200, and the hibonite-melilite partition coefficient is ~10.

In the type-B CAI, AXCAI-2775, fassaite is the main REE carrier. The fassaite has a LREE depleted pattern with La enriched ~15× and Lu enriched ~250× relative to CI and a large negative Eu anomaly (Fig. 7c). Melilite has a nearly flat pattern at ~10 × CI with

a positive Eu anomaly. The bulk REE patterns for AXCAI-2775 is relatively smooth, but fractionated, with La at ~10 × CI and Lu at ~100 × CI. In contrast to the melilite-rich CAIs, Tm and Yb in AXCAI-2775 are depleted relative to the adjacent elements (Fig. 7c).

Plagioclase-Bearing Chondrules–Figure 8 shows trace element and REE abundances for these chondrules. In AXCH-1471, pyroxene has a slightly fractionated REE pattern with HREEs enriched 2–3× relative to LREEs and a negative Eu anomaly (Fig. 8a). The REE abundances in pyroxene differ considerably across the chondrule. In the spinel-rich central region, HREEs are enriched 50–70× relative to CI; in the coarse-grained, spinel-free region, HREEs are enriched to 30–50 × CI; and in the finer-grained outer portion, HREEs are only enriched to 10–20 × CI. In contrast, Sc is most abundant in the outer portion (20–50 × CI) and decreases inward to ~4 × CI in the spinel-rich core (Fig. 8a). Plagioclase is relatively enriched in LREEs and has a large positive Eu anomaly. The bulk chondrule thus has a smooth pattern with La enriched ~6× and Lu enriched ~12× relative to CI. The REE and trace element variations within the chondrule are consistent with the following crystallization sequence. Pyroxene grains nucleated at the surface of the chondrule and grew rapidly inward, acquiring REEs at abundances similar to those of the bulk chondrule. This assumes that the pyroxene to liquid distribution coefficients for this composition are close to unity. Pyroxenes near the chondrule surface have high Sc contents (Fig. 8a), and Sc has a high pyroxene to liquid partition coefficient (*e.g.*, Davis *et al.*, 1990). As large amounts of plagioclase and olivine with low REEs began to crystallize, the REE abundance in the liquid increased, as reflected in the higher REE abundances of the interior pyroxene. Interior pyroxenes have low Sc contents, reflecting earlier Sc extraction by pyroxene.

In AXCH-1371, pyroxene has a relatively flat pattern with negative La and Eu anomalies and positive Tm and Yb anomalies (Fig. 8b). Pyroxene in the coarser-grained core has REE abundances 10–15 × CI, whereas pyroxene in the finer-grained exterior region is enriched to only 3–5 × CI. Plagioclase has low REE abundances, a fractionated pattern favoring LREEs, and a large positive Eu anomaly. Plagioclase may also be enriched in Yb relative to surrounding elements, mirroring the pyroxene. The bulk REE pattern is 3–4× enriched relative to CI, with a negative La anomaly, a positive Eu anomaly, slight depletions in Dy-Lu, and positive Tm and Yb anomalies. The pattern is similar to the muted Group II pattern in AXCAI-1571. The REE abundances in the minerals indicate a crystallization sequence similar to that inferred for AXCH-1471. However, Sc abundances increase from rim to core,

TABLE 5. Bulk composition of Axtell compared to that of Allende.

	Axtell*	Allende†
SiO_2	34.30	34.23
TiO_2	0.18	0.15
Al_2O_3	3.18	3.27
Cr_2O_3	0.49	0.52
Fe_2O_3	8.03	–
FeO	22.45	27.15
MnO	0.14	0.18
MgO	23.48	24.62
CaO	2.04	2.61
Na_2O	0.06	0.45
K_2O	0.02	0.03
P_2O_5	0.19	0.23
H_2O^+	0.85	<0.1
H_2O^-	2.51	0.00
Fe(m)	nm	0.17
Ni	0.42	0.36
Co	0.03	0.01
C	0.34	0.29
S	<0.1	–
FeS	–	4.03
Total	98.84	98.30
Total Fe	23.07	23.85

*E. Jarosewich, unpublished analysis.
†Clarke *et al.* (1970).
nm = not measured.

TABLE 6. Bulk compositions of Axtell chondrules and Al-rich objects from other meteorites.

	Axtell				Allende POIs*			Chainpur 5674-2-1†	Al-rich chondrule‡	Semarkona Type IA§
	AXCH-1471	AXCH-1371	AXCH-2171	AXCH-2272	5ALLB6	3510	B14D			
SiO_2	42.9	44.8	45.8	40.7	38.1	41.6	42.9	44.7	39.5–57.0	44.80
TiO_2	0.95	0.84	0.27	0.11	0.9	0.4	0.7	1.17	0.18–2.32	0.19
Al_2O_3	21.4	23.6	12.9	3.08	31.6	29.6	25.7	22.6	10.3–28.2	3.90
Cr_2O_3	0.30	0.17	0.36	0.26	0.6	0.3	0.2	0.22	0.07–1.39	0.44
FeO	0.55	0.26	1.16	2.23	0.6	1.5	1.6	0.90	0.43–14.5	1.18
MnO	0.04	0.02	0.15	0.04	nm	nm	nm	0.02	0.02–0.39	0.12
MgO	15.1	8.33	30.3	46.2	13.7	11.5	13.4	12.4	3.8–33.8	40.70
CaO	17.5	20.9	8.2	2.11	12.6	12.4	10.1	17.6	4.3–19.6	3.50
Na_2O	0.18	0.15	0.26	0.17	1.4	2.0	3.6	0.29	0.04–4.7	0.52
K_2O	0.02	0.02	0.02	0.02	nm	<0.1	0.1	0.01	0.02–0.36	0.07
V_2O_3	0.07	0.05	0.03	0.01	nm	nm	nm	0.01	nm	nm
NiO	0.02	0.03	0.05	0.03	nm	nm	nm	0.01	nm	–
Fe	–	–	–	3.84	–	–	–	–	–	–
Ni	–	–	–	0.29	–	–	–	–	–	–
Totals	99.03	99.17	99.50	99.09	99.5	99.3	98.3	99.93	–	99.38

*Sheng *et al.* (1991).
†Russell *et al.* (1996), Huss, unpubl. data.
‡Range for Al-rich chondrules described by Bischoff and Keil (1984).
§Mean composition of type-IA chondrules in Semarkona (Jones and Scott, 1989).
nm = not measured.

which suggests that anorthite, which does not take up Sc, played a larger role early in the crystallization sequence.

In AXCH-2171, REEs are sited primarily in the interstitial pyroxene (Fig. 5a). Pyroxene has a nearly flat pattern, ~60× enriched relative to CI, with a slight relative depletion of HREEs and a negative Eu anomaly (Fig. 8c). Plagioclase has roughly CI abundances of REEs, with a large positive Eu anomaly. Olivine has very low REE abundances and is particularly depleted in LREEs. The bulk pattern is 5–8× enriched with perhaps a slight relative depletion of HREEs.

In AXCH-2272, REEs are sited mainly in the interstitial pyroxene and plagioclase, but partitioning between phases is not as pronounced as in AXCH-2171 (Fig. 8c,d). Pyroxene exhibits a slight relative depletion in HREEs and a negative Eu anomaly. Plagioclase has a typical LREE-enriched patterns with a large positive Eu anomaly, but the REE abundance is remarkably high, with La ≈ 10 × CI, equal to the abundance in pyroxene. Olivine, which makes up ~80% of this chondrule (Table 1), has very low REE abundances. The bulk REE pattern is slightly fractionated favoring LREEs, and the REE abundances are roughly chondritic (Fig. 8d).

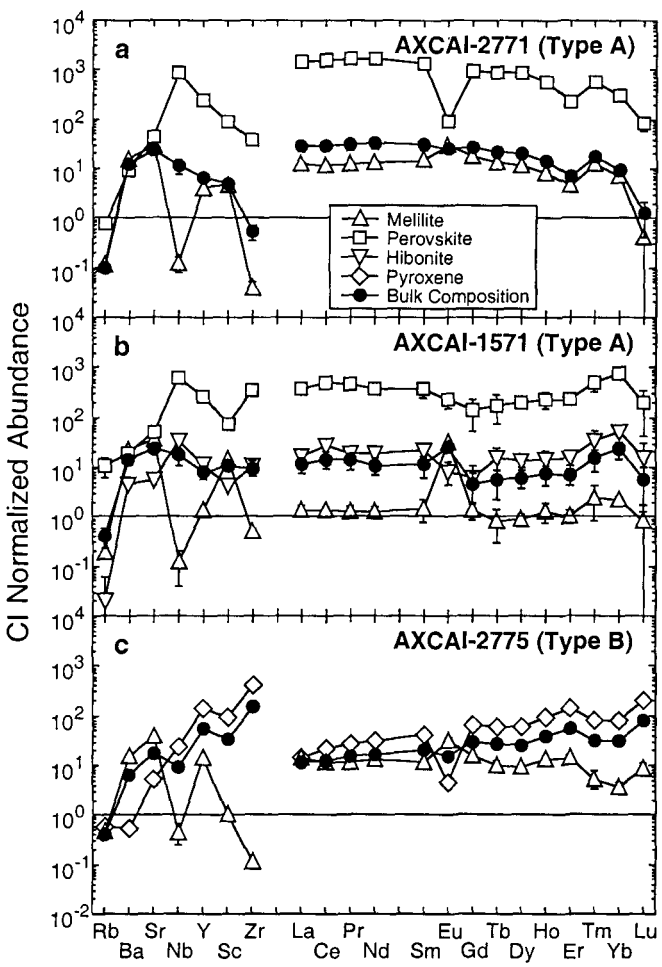

FIG. 7. Trace element and REE abundances for the Axtell CAIs normalized to CI abundances. Trace elements are arranged from most volatile on the left to most refractory on the right. Scandium and Zr are more refractory than the REEs. Mineral patterns are shown by open symbols and bulk patterns by filled symbols. Inclusions AXCAI-2771 (a) and AXCAI-1571 (b), both type-A inclusions, are enriched 10–20× in LREEs relative to CI abundances and show muted Group II bulk patterns with increasing relative depletions of Gd through Lu and positive Tm and Yb anomalies. The type-B inclusion, AXCAI-2775 (c), is enriched ~10× in LREEs relative to CI and has a relatively smooth sloping patterns with relative enrichment of HREEs and negative anomalies in Tm and Yb. All uncertainties are 2σ and those for bulk compositions include uncertainties in modal abundances.

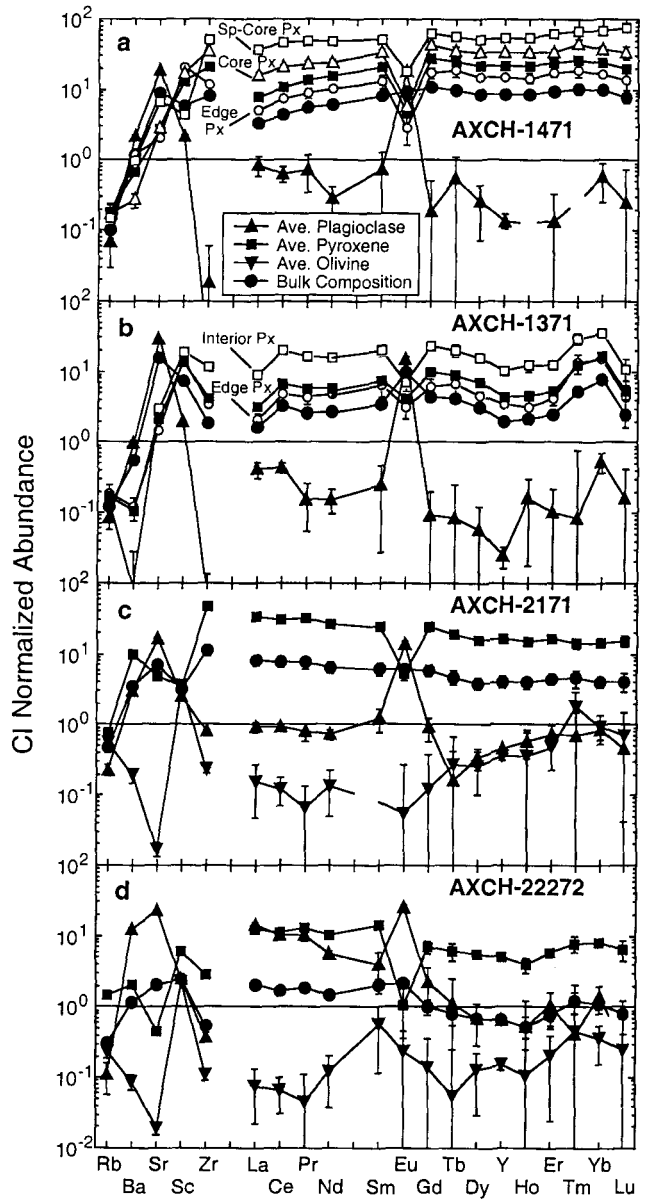

FIG. 8. Trace element and REE abundances for minerals in plagioclase-bearing chondrules and for the bulk chondrules (filled circles), all normalized to CI abundances. Trace elements are arranged from most volatile on the left to most refractory on the right. Scandium and Zr are more refractory than the REEs. For chondrules with large plagioclase laths (AXCH-1471 (a) and AXCH-1371 (b)), data are shown for pyroxene from different petrographic locations (open symbols). For these chondrules, core pyroxenes have higher REE abundances than those from near the chondrule edge. Bulk patterns of the three Al-rich chondrules are significantly enriched relative to CI chondrites. Chondrule AXCH-2272 (b) has roughly CI abundances of REEs. Chondrule AXCH-1371 (b) has a bulk REE pattern similar to the muted Group II pattern of AXCAI-1571, except for a positive Eu anomaly and a La depletion. In the barred-olivine chondrules, REEs are concentrated in the mesostasis, primarily in pyroxene. All uncertainties are 2σ and those for bulk compositions include uncertainties in modal abundances.

TABLE 7. Magnesium-aluminum data for Axtell CAIs and Al-rich chondrules.

Phase	F_{Mg}	$\delta^{26}Mg$	$^{27}Al/^{24}Mg$
AXCAI-2771			
Melilite 1	14.7 ± 2.1	3.0 ± 3.8	20.4 ± 1.0
Melilite 2	10.0 ± 1.6	1.0 ± 2.5	12.2 ± 0.6
Melilite 3	12.9 ± 2.5	3.2 ± 4.9	30.2 ± 1.5
Melilite 4	17.2 ± 2.3	0.9 ± 4.5	30.9 ± 1.6
Melilite 5	18.2 ± 1.9	−0.5 ± 3.3	24.0 ± 1.2
Melilite 6	15.4 ± 1.6	−0.0 ± 2.5	12.0 ± 0.6
Melilite 7	13.4 ± 1.5	0.4 ± 2.1	8.4 ± 0.4
Melilite 8	12.9 ± 1.5	−1.2 ± 2.1	8.0 ± 0.4
Melilite 9	14.0 ± 1.5	0.3 ± 2.1	7.8 ± 0.4
Melilite 10	18.9 ± 1.5	1.2 ± 2.7	21.5 ± 1.1
Spinel 1	14.2 ± 1.5	−0.5 ± 2.6	2.4 ± 0.1
Spinel 2	13.7 ± 1.3	−0.4 ± 2.2	2.4 ± 0.1
Spinel 3	17.2 ± 1.4	−0.6 ± 2.3	2.6 ± 0.1
Spinel 4	16.3 ± 1.4	−1.2 ± 2.4	2.5 ± 0.1
Hibonite 1	15.8 ± 1.5	−1.7 ± 2.7	20.5 ± 1.0
Hibonite 2	19.2 ± 1.5	−1.3 ± 2.8	29.5 ± 1.5
AXCAI-2571			
Melilite 1	12.6 ± 1.7	1.5 ± 2.9	13.0 ± 0.6
Melilite 2	13.2 ± 1.7	0.2 ± 2.6	12.0 ± 0.6
Melilite 3	14.1 ± 1.6	−0.5 ± 2.4	10.2 ± 0.5
Melilite 4	14.7 ± 1.4	−1.1 ± 1.8	4.7 ± 0.2
Melilite 5	15.1 ± 1.5	−0.4 ± 2.3	8.9 ± 0.4
Melilite 6	12.9 ± 1.5	1.3 ± 2.2	8.0 ± 0.4
Melilite 7	14.4 ± 1.2	−0.8 ± 2.0	5.7 ± 0.2
Spinel 1	12.6 ± 1.1	−0.0 ± 2.1	2.4 ± 0.1
Spinel 2	12.7 ± 1.4	1.1 ± 2.4	2.4 ± 0.1
Spinel 3	14.8 ± 1.4	−1.5 ± 2.5	2.5 ± 0.1
Hibonite	17.1 ± 1.7	0.5 ± 3.1	25.8 ± 1.3
AXCAI-2271			
Melilite 1	13.2 ± 1.7	−0.4 ± 2.8	17.4 ± 0.9
Melilite 2	12.8 ± 1.5	0.4 ± 2.3	17.7 ± 0.9
Melilite 3	12.9 ± 1.6	0.2 ± 2.4	13.8 ± 0.7
Melilite 4	12.5 ± 1.6	1.1 ± 2.4	13.2 ± 0.7
Melilite 5	12.0 ± 1.7	4.1 ± 2.9	25.4 ± 1.3
Melilite 6	15.4 ± 1.7	1.4 ± 2.9	20.2 ± 1.0
Melilite 7	15.6 ± 1.8	−0.6 ± 3.0	22.4 ± 1.1
Melilite 8	11.6 ± 1.5	0.3 ± 2.1	17.4 ± 0.9
Melilite 9	16.1 ± 1.7	−0.6 ± 2.8	20.0 ± 1.0
Melilite 10	15.9 ± 2.6	−3.2 ± 5.1	29.5 ± 1.5
Spinel 1	13.1 ± 1.2	1.5 ± 2.0	2.5 ± 0.1
Spinel 2	14.1 ± 1.3	−0.2 ± 2.1	2.5 ± 0.1
AXCAI-1571			
Melilite 1	4.3 ± 2.1	12.0 ± 3.9	29.6 ± 1.6
Melilite 2	4.5 ± 1.8	8.6 ± 3.2	21.4 ± 1.1
Melilite 3	4.5 ± 1.7	9.3 ± 3.0	20.2 ± 1.1
Melilite 4	4.4 ± 1.6	3.6 ± 2.6	10.7 ± 0.5
Melilite 5	5.4 ± 2.0	10.4 ± 3.7	29.7 ± 1.5
Melilite 6	2.3 ± 1.6	6.5 ± 2.4	12.1 ± 0.6
Melilite 7	3.4 ± 1.8	8.4 ± 3.1	20.2 ± 1.0
Spinel 1	2.4 ± 1.7	1.2 ± 3.2	2.9 ± 0.1
Spinel 2	3.1 ± 1.5	1.8 ± 2.7	2.6 ± 0.1
AXCAI-2775			
Melilite 1	3.0 ± 1.5	4.5 ± 2.3	13.8 ± 0.7
Melilite 2	6.4 ± 1.4	3.8 ± 1.8	8.7 ± 0.5
Melilite 3	3.6 ± 1.5	5.2 ± 2.2	10.4 ± 0.5
Melilite 4	4.0 ± 1.4	3.4 ± 2.0	9.9 ± 0.5
Spinel	3.3 ± 1.2	0.6 ± 2.0	2.6 ± 0.1
Pyroxene	7.5 ± 0.8	0.6 ± 1.6	2.3 ± 0.1
Plagioclase	−8.3 ± 5.5	4.7 ± 11.3	1333 ± 70
AXCH-1471			
Olivine 1	−0.1 ± 1.0	0.9 ± 2.1	0.0078 ± 0.0006
Olivine 2	1.8 ± 0.8	1.1 ± 1.6	0.0013 ± 0.0001
Olivine 3	1.4 ± 0.7	2.0 ± 1.4	0.0013 ± 0.0004
Spinel 1	2.8 ± 1.3	1.7 ± 2.2	2.4 ± 0.1
Spinel 2	2.7 ± 1.3	1.2 ± 2.0	2.6 ± 0.1
Spinel 3	4.9 ± 1.2	0.7 ± 1.9	2.6 ± 0.1
Spinel 4	4.4 ± 1.2	0.5 ± 1.9	2.6 ± 0.1
Fe-rich Spinel 1	4.3 ± 1.2	1.1 ± 1.9	2.8 ± 0.1
Fe-rich Spinel 2	5.4 ± 1.2	−1.1 ± 2.0	2.7 ± 0.1
Fe-rich Spinel 3	4.6 ± 1.2	0.5 ± 1.9	2.8 ± 0.1
Pyroxene 1	3.0 ± 0.9	1.0 ± 1.9	0.24 ± 0.01
Pyroxene 2	3.5 ± 0.9	1.8 ± 1.8	0.39 ± 0.02
Plagioclase 1	0.4 ± 2.4	4.4 ± 3.1	109.5 ± 5.7
Plagioclase 2	1.8 ± 2.4	5.2 ± 3.4	115.2 ± 5.8
Plagioclase 3	−0.2 ± 2.6	5.7 ± 4.1	165.2 ± 8.3
Plagioclase 4	2.3 ± 2.4	1.1 ± 3.6	131.8 ± 6.7
Plagioclase 5	−2.1 ± 2.7	3.0 ± 4.5	150.4 ± 7.6
Plagioclase 6	0.9 ± 2.5	5.4 ± 3.9	144.8 ± 7.3
Plagioclase 7	0.9 ± 2.4	5.7 ± 3.5	122.3 ± 6.2
Plagioclase 8	1.2 ± 2.4	3.0 ± 3.5	118.1 ± 5.9
AXCH-1371			
Olivine 1	–	−0.6 ± 0.9	0.0020 ± 0.0001
Plagioclase 1	–	0.4 ± 3.4	144.2 ± 7.3
Plagioclase 2	–	−2.1 ± 3.7	127.1 ± 6.4
Plagioclase 3	–	1.9 ± 6.0	228.1 ± 11.5
Plagioclase 4	–	3.0 ± 5.1	184.0 ± 9.3
Plagioclase 5	–	2.1 ± 5.5	200.5 ± 10.1
Pyroxene 1	–	−0.9 ± 0.8	0.509 ± 0.025
AXCH-2171			
Olivine 1	–	−0.1 ± 1.0	0.0010 ± 0.0001
Plagioclase 1	–	−1.8 ± 3.1	33.5 ± 2.1
Plagioclase 2	–	−0.3 ± 3.5	44.6 ± 2.4
Plagioclase 3	–	−1.0 ± 4.9	83.1 ± 4.2
Plagioclase 4	–	−0.3 ± 4.3	88.9 ± 4.5
Plagioclase 5	–	−2.0 ± 6.0	85.8 ± 4.7
Plagioclase 6	–	−1.1 ± 4.7	56.2 ± 3.0
Plagioclase 7	–	−0.4 ± 3.3	60.9 ± 3.1
Plagioclase 8	–	−1.1 ± 2.6	22.6 ± 1.1
Plagioclase 9	–	0.9 ± 2.4	29.0 ± 1.5
Plagioclase 10	–	−1.3 ± 3.6	66.8 ± 3.4
Plagioclase 11	–	−0.8 ± 4.4	69.9 ± 3.5
Plagioclase 12	–	2.2 ± 4.3	75.0 ± 3.8
AXCH-2272			
Olivine 1	–	−0.5 ± 1.8	0.0005 ± 0.0001
Plagioclase 1	–	−1.8 ± 6.8	56.2 ± 2.8
Plagioclase 2	–	9.4 ± 7.0	65.9 ± 3.3
Plagioclase 3	–	−3.7 ± 3.8	20.5 ± 1.0
Plagioclase 4	–	3.3 ± 4.7	28.9 ± 1.5
Plagioclase 5	–	3.6 ± 5.5	39.8 ± 2.0
Plagioclase 6	–	0.3 ± 3.1	6.2 ± 0.3
Plagioclase 7	–	0.7 ± 3.5	15.1 ± 0.8
Plagioclase 8	–	1.3 ± 3.3	12.2 ± 0.6

All error bars are $2\sigma_{mean}$.

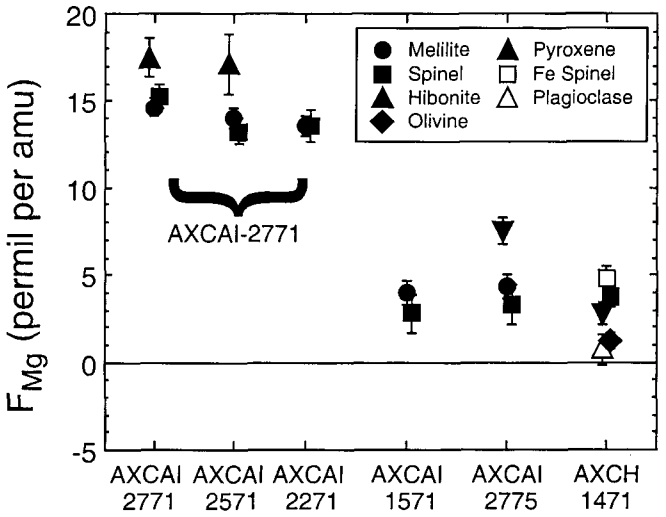

FIG. 9. The degree of mass fractionation in Mg (F_{Mg}) is plotted for several minerals in each of the Axtell CAIs and in chondrule AXCH-1471. Plotted data are averages of the measured values from Table 7. Inclusion AXCAI-2771 is highly fractionated favoring heavy isotopes, with melilite and spinel exhibiting F_{Mg} of ~14‰/amu and hibonite showing a somewhat larger value. The hibonite is located near the edge of the inclusion and may reflect isotopic evolution of the surface layer during crystallization. The other two CAIs and AXCH-1471 are slightly fractionated favoring the heavy isotopes and exhibit F_{Mg} values similar to those for most Allende CAIs.

ISOTOPIC RESULTS

Magnesium

Magnesium-isotopic compositions are given in Table 7. In the large melilite-rich CAI, AXCAI-2771, Mg is fractionated 14–18‰/amu favoring the heavy isotopes for all phases (Fig. 9). Hibonite has a higher F_{Mg} than melilite and spinel, which suggests a multi-stage origin. Mass fractionation of this magnitude is characteristic of the rare and isotopically highly anomalous FUN inclusions in Allende (*e.g.*, Wasserburg *et al.*, 1977). Inclusions AXCAI-1571 and AXCAI-2775 are fractionated 3–5‰ (Fig. 9), like most CAIs from other meteorites (Esat and Taylor, 1984, Clayton *et al.*, 1988, MacPherson *et al.*, 1988, Goswami *et al.*, 1994). Quantitative F_{Mg} data were only obtained for one chondrule, AXCH-1471, where pyroxene and spinel (independent of Fe content) are fractionated to about +4‰, whereas olivine appears to be unfractionated.

The large type-A CAI (AXCAI-2771) shows no resolved $^{26}Mg^*$ and gives an upper limit for $(^{26}Al/^{27}Al)_0$ of $<1.1 \times 10^{-5}$ (Fig. 10a). Low $(^{26}Al/^{27}Al)_0$ is again characteristic of FUN inclusions (Wasserburg *et al.*, 1977; Lee *et al.*, 1979). Two CAIs exhibit clear excesses of $^{26}Mg^*$. Inclusion AXCAI-1571 exhibits a good correlation between $^{27}Al/^{24}Mg$ and $^{26}Mg/^{24}Mg$, and the inferred $(^{26}Al/^{27}Al)_0$ is $\sim 5 \times 10^{-5}$ (Fig. 10b). The type-B CAI, AXCAI-2775, exhibits complicated Al-Mg systematics. Spinel, pyroxene, and melilite show a reasonable correlation between $^{27}Al/^{24}Mg$ and $^{26}Mg^*$ with $(^{26}Al/^{27}Al)_0 \approx 5 \times 10^{-5}$ (Fig. 11). However, a plagioclase crystal with $^{27}Al/^{24}Mg \approx 1300$ does not have a resolvable excess of $^{26}Mg^*$. A regression of spinel, pyroxene, and plagioclase gives $(^{26}Al/^{27}Al)_0 < 1.6 \times 10^{-6}$ (Fig. 11, inset). This situation was also reported for Efremovka type-B1 inclusion E44 (Goswami *et al.*, 1994). The very high $^{27}Al/^{24}Mg$ and the low $(^{26}Al/^{27}Al)_0$ of the plagioclase and the polygranular texture of the melilite indicate that AXCAI-2775 has been metamorphosed. Anorthite and melilite have similar $^{26}Mg/^{24}Mg$ ratios (Fig. 11), which suggests that the two minerals have equilibrated.

One Al-rich chondrule, AXCH-1471, shows a small but well defined excess of $^{26}Mg^*$ in plagioclase and an inferred $(^{26}Al/^{27}Al)_0 = (3.4 \pm 1.5) \times 10^{-6}$ (Fig. 12a). Plagioclase in AXCH-1371 did not show a resolved $^{26}Mg^*$ despite $^{27}Al/^{24}Mg$ ratios of up to 225. The upper limit on $(^{26}Al/^{27}Al)_0$ is $<3 \times 10^{-6}$ (Fig. 12b). Likewise, the plagioclase-bearing barred-olivine chondrules, AXCH-2272 and AXCH-2171, do not show clear evidence of ^{26}Al (Fig. 12c,d).

TABLE 8. Titanium isotopes in perovskite from AXCAI-2571 (AXCAI-2771).

	F_{Ti} (‰/amu)	$\delta^{47}Ti$	$\delta^{49}Ti$	$\delta^{50}Ti$
Standard	–	−0.1 ± 0.6	−1.1 ± 0.6	−0.3 ± 0.7
Per. #1	1.7 ± 0.9	−0.3 ± 0.8	−1.0 ± 0.9	3.2 ± 1.0
Per. #2	5.2 ± 1.4	1.1 ± 1.4	−1.0 ± 1.4	3.6 ± 1.9
Mean	2.5 ± 0.1	0.1 ± 0.7	−1.0 ± 0.7	3.3 ± 0.9

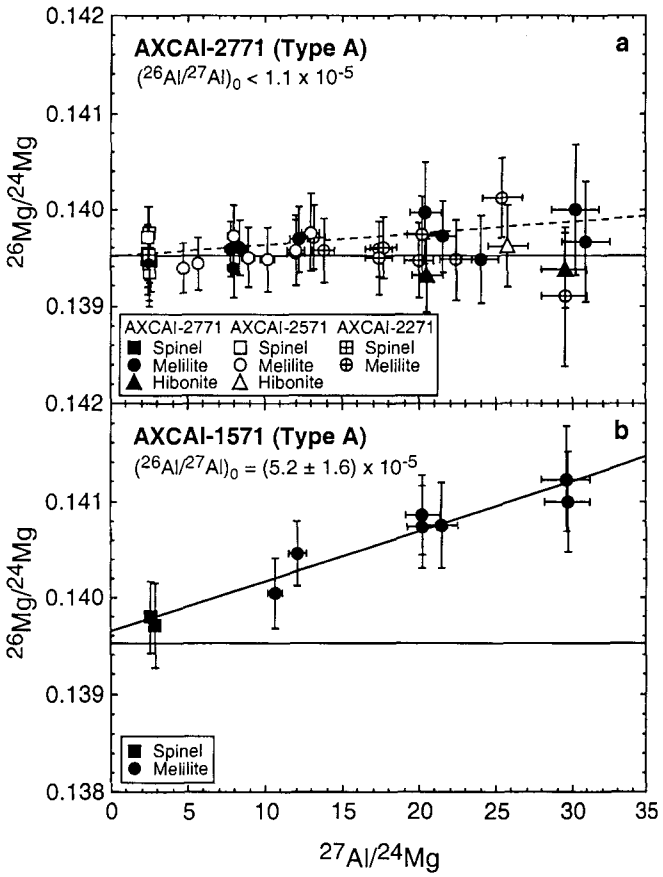

FIG. 10. Evolution diagrams of Mg-Al for the type-A CAIs AXCAI-2771 and AXCAI-1571. (a) Data for all three pieces of AXCAI-2771 are shown. These data do not show a resolved excess of $^{26}Mg^*$ and the inferred $(^{26}Al/^{27}Al)_0$ is $<1.1 \times 10^{-5}$. (b) Magnesium data for melilite and spinel in AXCH-1571 show a good correlation with Al/Mg indicating that ^{26}Al decayed *in situ*. The inferred $(^{26}Al/^{27}Al)_0$ is $\sim 5 \times 10^{-5}$, similar to the values observed in many unaltered CAIs from other meteorites.

Titanium

Because the Al-Mg characteristics of AXCAI-2771 ($F_{Mg} \approx 15$–18‰; $(^{26}Al/^{27}Al)_0 < 1.1 \times 10^{-5}$) are similar to those of FUN inclusions, we measured Ti isotopes in some large perovskite grains. The Ti isotopes are mass fractionated favoring the heavy isotopes,

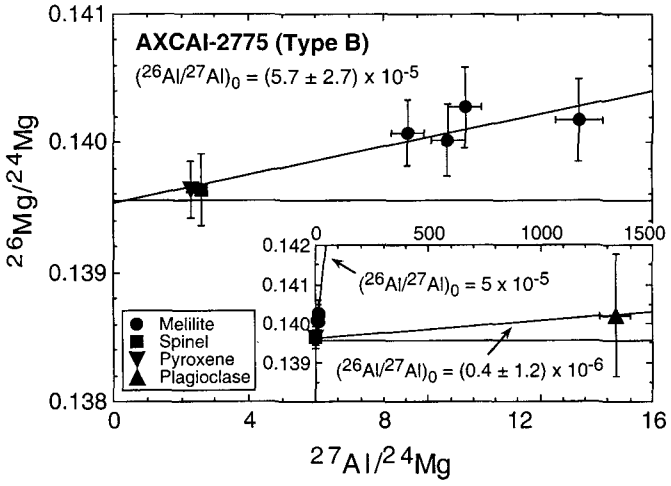

FIG. 11. Evolution diagram of Mg-Al for the type-B CAI AXCAI-2775. This inclusion shows complicated Mg-Al systematics. Data for pyroxene, spinel, and melilite show a reasonable correlation with Al/Mg and give an inferred $(^{26}Al/^{27}Al)_0$ of ~5 × 10^{-5}. However, plagioclase, which has a $^{27}Al/^{24}Mg$ ratio of ~1300, shows no evidence of $^{26}Mg^*$ and gives an inferred $(^{26}Al/^{27}Al)_0$ of <1.6 × 10^{-6}. These data are consistent with metamorphic remobilization of Mg at a time after ^{26}Al decayed.

with $F_{Ti} \approx 2.5‰$, and there is a clearly resolved ~3.3‰ excess at ^{50}Ti (Table 8; Fig. 13). This excess is similar to that observed in the FUN inclusion, EK-1-4-1 (Niederer *et al.*, 1981), and suggests that AXCAI-2771 is indeed a FUN inclusion.

DISCUSSION

To successfully interpret the data on CAIs and chondrules from Axtell and to place these data in the broader context of chondritic meteorites, it is necessary to understand the history of the individual objects prior to accretion, the history of the Axtell meteorite, and the histories of the meteorites to which we wish to compare our results. One must first recognize and account for alteration that took place in the meteorite parent body. Comparisons with Allende may be particularly instructive.

The CV3 chondrites have been divided into oxidized (*e.g.*, Allende, Axtell, Ningqiang, Bali, Grosnaja, Mokoia, and Kaba) and reduced subgroups (*e.g.*, Leoville, Vigarano, and Efremovka) (McSween, 1977). Further subdivision of the oxidized subgroup was suggested by Weisberg *et al.* (1997), who placed Allende, Axtell, and Ningqiang in the $CV3_{OxA}$ subgroup and Bali, Grosnaja, Mokoia, and Kaba in the $CV3_{OxB}$ subgroup. Oxidized CV3 chondrites have little or no metallic Fe and generally have higher contents of Mn, Fe, Na, K, and Br than reduced CV3 chondrites (*e.g.*, Krot *et al.*, 1995). The $CV3_{OxB}$ chondrites contain widespread phyllosilicates that replace primary minerals in chondrules and CAIs (*e.g.*, Krot *et al.*, 1995; Weisberg *et al.*, 1997). The constituents of

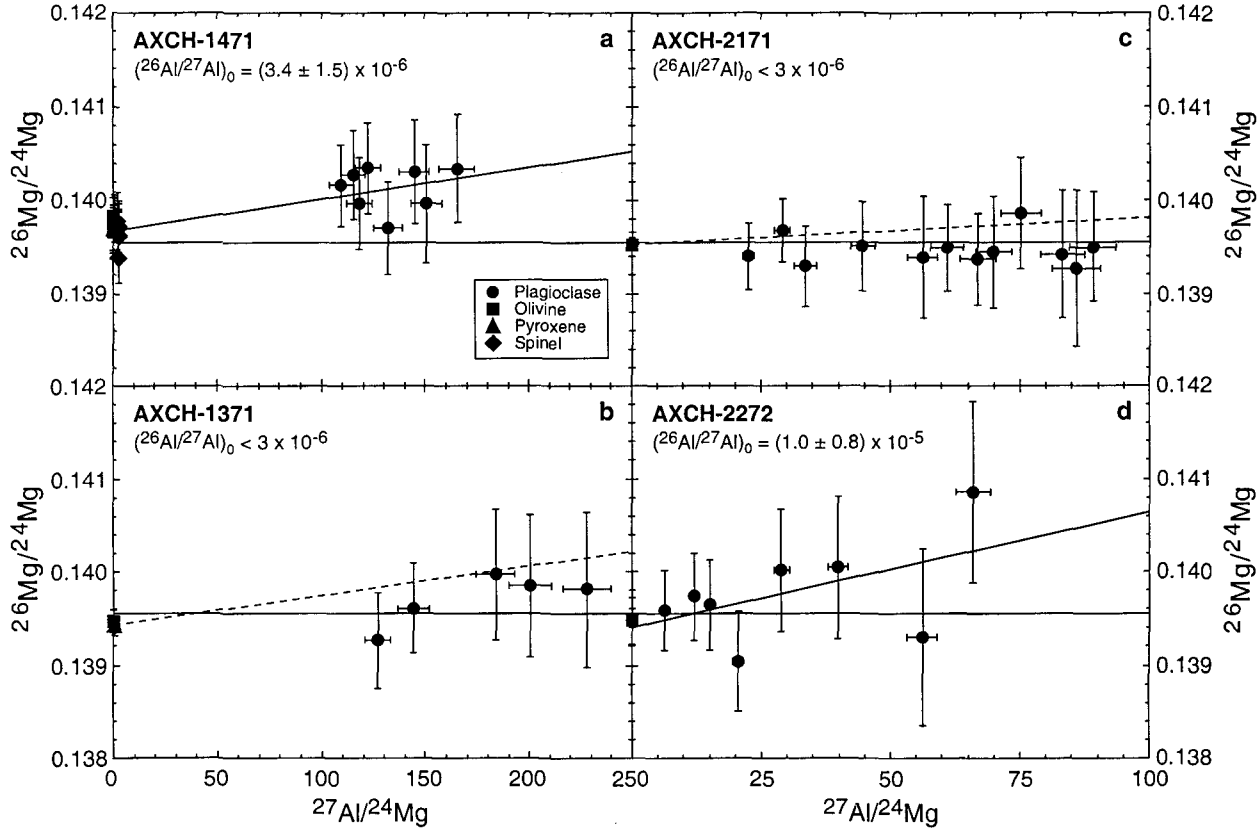

FIG. 12. Evolution diagrams of Mg-Al for Al-rich chondrules from Axtell. For AXCH-1471 (a), plagioclase exhibits a small excess of ^{26}Mg and the $^{26}Mg/^{24}Mg$ ratios for olivine, pyroxene, spinel, and plagioclase correlate with Al/Mg ratio. The inferred $(^{26}Al/^{27}Al)_0$ is ~3 × 10^{-6}. Chondrule AXCH-1371 (b) shows no evidence of excess $^{26}Mg^*$. The upper limit on the inferred $(^{26}Al/^{27}Al)_0$ is <3 × 10^{-6}. For AXCH-2171(c), data for olivine and plagioclase show no evidence of $^{26}Mg^*$. The upper limit on the inferred $(^{26}Al/^{27}Al)_0$ is <3 × 10^{-6}. For AXCH-2272 (d), data for olivine and plagioclase show only a hint of the presence of $^{26}Mg^*$ and the inferred $(^{26}Al/^{27}Al)_0$ is limited to <2 × 10^{-5}.

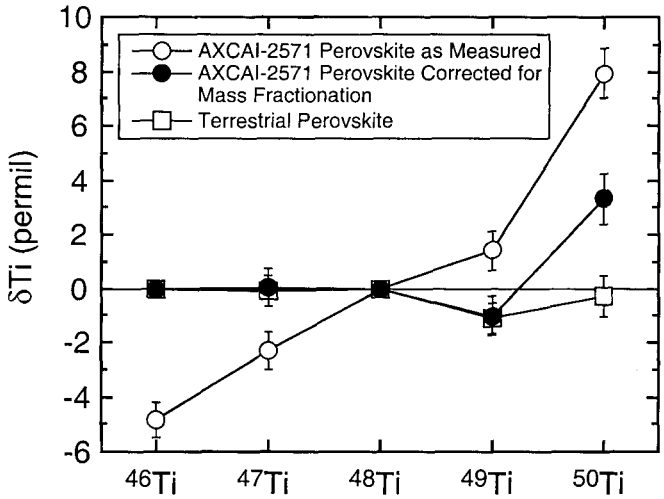

FIG. 13. Titanium isotopic data for perovskite in type-A inclusion AXCAI-2771. The Ti isotopes are mass fractionated favoring heavy isotopes with respect to terrestrial Ti, with $F_{Ti} \approx 2.5$‰/amu (shown by the open circles). When corrected for mass fractionation using ^{46}Ti and ^{48}Ti (filled circles), there is a clearly resolved nonlinear excess at ^{50}Ti of ~3.3‰. These characteristics are consistent with the identification of AXCAI-2771 as a FUN inclusion.

all oxidized CV3 chondrites have experienced various degrees of low-temperature (<1000 K) metasomatic alteration, which produced grossular, anorthite, ilmenite, nepheline, sodalite, hedenbergite, and other minerals from primary phases through introduction of alkalis, halogens, and Fe (Krot *et al.*, 1995). Many authors infer that this metasomatism occurred prior to accretion (*e.g.*, Grossman *et al.*, 1975; MacPherson *et al.*, 1988). Constituents of reduced CV3 chondrites experienced less of this metasomatism. Parent-body metamorphism also affected the CV3 chondrites to varying degrees. Allende exhibits the smallest spread in fayalite content of matrix olivines among oxidized CV3 chondrites and thus may have experienced the highest metamorphic temperatures (McSween, 1977; Krot *et al.*, 1995). Estimates for the maximum temperature experienced by Allende range from ~350 to ~550 °C (Krot *et al.*, 1995, and references therein).

Axtell and Allende, both $CV3_{OxA}$ chondrites, have had similar pre- and post-accretionary histories. The CAIs and chondrules in both meteorites have been extensively metasomatized, but Axtell has much lower bulk Na and S contents than Allende (Table 5), and its CAIs are not as strongly sulfidized (Simon *et al.*, 1995), implying a lower degree of metasomatism. Axtell may also be somewhat less metamorphosed than Allende. Matrix olivines in Axtell show a larger compositional range than in Allende (Krot *et al.*, 1995), and Axtell has a slightly higher abundance of presolar silicon carbide in its matrix (Huss *et al.*, 2000). But these differences are second order—constituents of both meteorites are extensively altered.

Axtell and Allende contain similar suites of CAIs, including type-B1, type-B2, compact type-A, and fine-grained varieties (Simon *et al.*, 1994, 1995; this study). However, there are subtle differences in mineralogy and mineral chemistry (also see Simon *et al.*, 1994). For example, fassaite in one Axtell type-B CAI is more Ti-rich than that in most Allende type-B inclusions (see Petrography and Mineral Chemistry, Calcium-Aluminum-Rich Inclusions), and the bulk is more Al- and Ti-rich than most Allende type-B inclusions (Table 4). Both of the compact type-A inclusions described here have subdued Group II REE patterns. Although Group II patterns are known from compact type-A Allende inclusions, most Group II inclusion in Allende are fine-grained and spinel rich, and most compact type-A inclusion have different REE patterns (*e.g.*, MacPherson *et al.*, 1988). Axtell and Allende both contain CAIs with $(^{26}Al/^{27}Al)_0 \approx 5 \times 10^{-5}$ and $F_{Mg} \approx 3$‰/amu. In both meteorites, later heating has partially redistributed Mg isotopes in some inclusions (Fig. 11; Podosek *et al.*, 1991). One Axtell CAI, AXCAI-2771, is highly mass fractionated, exhibits a ^{50}Ti excess, and does not contain detectable $^{26}Mg^*$. This inclusion is thus similar in several respects to the Allende FUN inclusion EK1-4-1 (*e.g.*, Niederer *et al.*, 1981). The Axtell CAI, "Porky", studied by Caillet and Zinner (1995), has an even larger excess of ^{50}Ti (~62‰) accompanied by excess ^{48}Ca (~38‰) and no detectable $^{26}Mg^*$, although Mg in "Porky" is not mass fractionated. Two highly anomalous inclusions out of four studied to date may indicate a high proportion of isotopically anomalous inclusions in Axtell. These comparisons indicate that Axtell contains a distinct suite of CAIs but that the range of characteristics found is similar to that observed in Allende and in other CV meteorites.

Two Axtell plagioclase-pyroxene chondrules (AXCH-1471 and AXCH-1371) are similar in mineralogy and texture to Group 1 POIs from Allende (Sheng *et al.*, 1991). Two Allende POIs exhibited $^{26}Mg^*$ with $(^{26}Al/^{27}Al)_0 = 6.1 \times 10^{-6}$ and 2.6×10^{-6} (Sheng *et al.*, 1991), and a similar value was obtained for AXCAI-1471 ($\sim 3 \times 10^{-6}$). Other chondrules in both meteorites do not show evidence of ^{26}Al, but the limits on $(^{26}Al/^{27}Al)_0$ are comparable with the detections.

Constraints on Nebular Timescales

The CAIs and plagioclase-bearing chondrules in Axtell exhibit the complete range of $(^{26}Al/^{27}Al)_0$ values observed in Allende and other meteorites. Metamorphism in the Axtell parent body cannot be responsible for the range of initial ratios for Axtell CAIs. Two melilite-rich CAIs, AXCAI-2771 and AXCAI-1571, both contain melilite with Al/Mg ratios of ~30, but one gives $(^{26}Al/^{27}Al)_0 \approx 5 \times 10^{-5}$, whereas the other shows $(^{26}Al/^{27}Al)_0 < 1 \times 10^{-5}$ (Fig. 10). If both inclusions had experienced the same metamorphic event, that event should have reset the melilite in both inclusions to about the same extent. Inclusion AXCAI-2775 (type-B) may have experienced higher temperatures than the two type-A inclusions, as indicated by the polygranular texture of the melilite and the apparent Mg-isotopic exchange between anorthite and melilite (Fig. 11). Plagioclase in one Al-rich chondrule (AXCH-1471) has $(^{26}Al/^{27}Al)_0 \approx 3 \times 10^{-6}$, whereas another (AXCH-1371) does not have resolved $^{26}Mg^*$ excesses in spite of higher Al/Mg ratios (Fig. 12). The preservation of $^{26}Mg^*$ excesses in AXCH-1471, combined with the Mg self-diffusion rate for anorthite (LaTourrette and Wasserburg, 1998), appear to limit the maximum temperature of metamorphism on the Axtell parent body to ~600 °C. This is consistent with the limit derived from noble gases in presolar diamonds from Axtell (Huss *et al.*, 2000) and with comparisons to Allende. The apparent equilibration of plagioclase and melilite in AXCAI-2775 indicates that some constituents of Axtell experienced higher temperatures than the bulk meteorite.

Similarly diverse $(^{26}Al/^{27}Al)_0$ values are observed in suites of objects in other CV3 chondrites. For example, Allende contains anorthite-bearing type-B CAIs with clearly resolved $^{26}Mg^*$ with $(^{26}Al/^{27}Al)_0 \approx 5 \times 10^{-5}$ (*e.g.*, WA, Lee *et al.*, 1977) and FUN inclusions with little or no evidence of ^{26}Al (*e.g.*, Lee *et al.*, 1979). Inclusions with $^{26}Mg^*$ but with disturbed Al-Mg systematics are also observed (*e.g.*, Podosek *et al.*, 1991). Allende also contains POIs with $(^{26}Al/^{27}Al)_0 \approx 3 \times 10^{-6}$ and others with no evidence of

$^{26}Mg^*$ (Sheng *et al.* 1991). In Efremovka, a reduced CV3, a plagioclase-bearing type-B CAI, E44, exhibits a disparity between spinel-melilite and spinel-anorthite regressions similar to that in AXCAI-2775 (Goswami *et al.*, 1994). However, in other plagioclase-bearing CAIs from Efremovka, plagioclase gives $(^{26}Al/^{27}Al)_0 = (3–4) \times 10^{-5}$. The presence of inclusions with similar mineral assemblages and variable $(^{26}Al/^{27}Al)_0$ values in the same meteorite would seem to preclude the meteorite parent body as the site of metamorphism. Similar arguments were made by Russell *et al.* (1996) for Chainpur (LL3.4), which has highly unequilibrated silicates in both chondrules and matrix (Huss *et al.*, 1981). The wide range of histories apparently experienced by individual objects within lightly metamorphosed meteorites shows that the constituents of chondrites had extended histories before they were incorporated into the final meteorite parent bodies.

If CAIs and chondrules were produced from a single isotopically homogeneous reservoir, then the range of $(^{26}Al/^{27}Al)_0$ values reflect differences in time of formation or latest significant alteration. The implied timescale is several million years from the first formation of CAIs to accretion of meteorite parent bodies (*e.g.*, Russell *et al.*, 1996). Two main issues arise from this interpretation. First, theoretical models indicate that chondrule-sized to meter-sized objects have short characteristic lifetimes (10^3 to 10^5 years) in the solar nebula because of gas drag (*e.g.*, Cameron, 1995). It follows that in order to preserve small objects formed over timescales of a few million years, they must be rapidly accumulated into planetesimals and stored there. The second issue is to understand why a few inclusions, such as FUN inclusions and some hibonite microspherules, carry little or no evidence of ^{26}Al, and thus presumably formed late, but yet carry some of the largest isotopic anomalies in Ca and Ti, which apparently reflect incomplete mixing of presolar components (*e.g.*, MacPherson *et al.*, 1995).

These issues have led to various nonchronological interpretations. For example, one way to resolve the FUN inclusion problem is to call on isotopic heterogeneity in the nebula and to propose that CAIs with different characteristics formed at approximately the same time from different packets of material (*e.g.*, Lee *et al.*, 1979). However, it is difficult to maintain large-scale spatial isotopic heterogeneity over the timescales required for a molecular cloud to collapse, an accretion disk to form, and for chondrules and CAIs to be produced, when all of these processes work toward homogenizing the isotopic composition.

As an alternative, Wood (1996) suggested that, because ^{26}Al was recently synthesized, it would have been primarily sited in a component of the presolar dust that was more volatile than that which carried the majority of the Al. In contrast, anomalous Ca and Ti would have been sited primarily in older refractory presolar stellar materials. This is because most dust is repeatedly evaporated and recondensed in interstellar space and only refractory grains would survive to preserve stellar signatures. Bulk presolar dust had $^{26}Al/^{27}Al \approx 5 \times 10^{-5}$ and Ca and Ti had normal isotopic compositions. Normal CAIs are proposed to have formed from bulk nebular material. As volatile material containing ^{26}Al and isotopically normal Ca and Ti evaporated, refractory dust with little ^{26}Al and anomalous Ca and Ti would remain. The FUN inclusions are interpreted to have formed by melting the residual solids after evaporation of much of the dispersed dust. The model proposed by Wood (1996) cannot easily explain low $(^{26}Al/^{27}Al)_0$ in chondrules because their bulk compositions require that they contain a significant fraction of the less refractory, ^{26}Al-rich component of nebular dust. But chondrules could have formed later.

Origin of Aluminum-Rich Chondrules

Aluminum-rich chondrules are unusual in that they have very much higher Al_2O_3 and CaO contents than typical chondrules (*e.g.*, type-IA chondrules, Table 6). Their Al_2O_3 and CaO contents are intermediate between those of CAIs (Table 4) and ferromagnesian chondrules (Table 6; Jones and Scott, 1989), but these three classes of objects do not form a linear trend on a Ca–Mg–Al–Si (CMAS) diagram (*e.g.*, Russell *et al.*, 1996). In this section, we investigate three possible mechanisms by which Al-rich chondrules might have originated: (1) Al-rich compositions may have been produced by igneous fractionation, (2) chondrules may have become Al-rich by incorporating a CAI fragment or other Al-rich material, and (3) Al-rich chondrules may have formed from residues of evaporation of normal chondritic material. Other more complex, multi-stage processes can be envisioned, but we limit ourselves to these three possibilities.

Igneous Fractionation–Aluminum-rich compositions might be produced by fractional crystallization of a chondritic melt, with chondrules produced from the fractionated melt. A subset of possible compositions produced by igneous fractionation would fall, on appropriate phase diagrams, at invariant points where the liquid is multiply saturated. More generally, a group of compositions related by a single process would fall along an array on the diagrams. We have plotted the compositions of Al-rich chondrules on phase diagrams of the CMAS system (Sheng, 1992). Oxides of the CMAS system comprise 96–97.5% of the mass of the chondrules.

The plagioclase-pyroxene chondrules, AXCH-1471 and AXCH-1371, are adequately represented by a four-component subset of the CMAS system, diopside–tridymite–spinel–anorthite. A four-component system can be plotted on a ternary diagram by projecting the compositions from the fourth component, which is typically the liquidus phase (*e.g.*, Stolper, 1982). We have plotted compositions of AXCH-1471 and AXCH1371 and Al-rich chondrules from Sheng *et al.* (1991) on the diagram diopside–tridymite–spinel projected from anorthite (Fig. 14). Figure 14 shows the phase boundaries and the anorthite saturation surface, and the number in parentheses next to each data point is the corresponding An coordinate. If the An coordinate is larger than the nearby contours of the anorthite saturation surface, then the bulk composition lies above that surface and anorthite was the liquidus phase. Chondrule AXCH-1471 projects very near to the boundary between An + Fo + L and An + Sp + L. Its An coordinate places it within uncertainties of the anorthite saturation surface (Fig. 14). However, a small amount of Na or Fe can have a large effect on the inferred phase composition (Sheng, 1992). When projected from both albite and anorthite, the composition falls farther from tridymite in the An + Sp + L field and the An coordinate places it below the anorthite saturation surface (Fig. 14). Spinel is then the liquidus phase, which is consistent with the textural evidence (Fig. 3). Projecting from fayalite to account for the small amount of Fe pushes the composition farther from tridymite. Chondrule AXCH-1371 projects onto the boundary between the An + Cpx + L and An + Fo + L fields, and its An coordinate places it well above the anorthite saturation surface (Fig. 14). Thus, anorthite is the expected liquidus phase. Projecting from albite and fayalite moves the composition away from tridymite to a position slightly off the diagram and lowers the An coordinate.

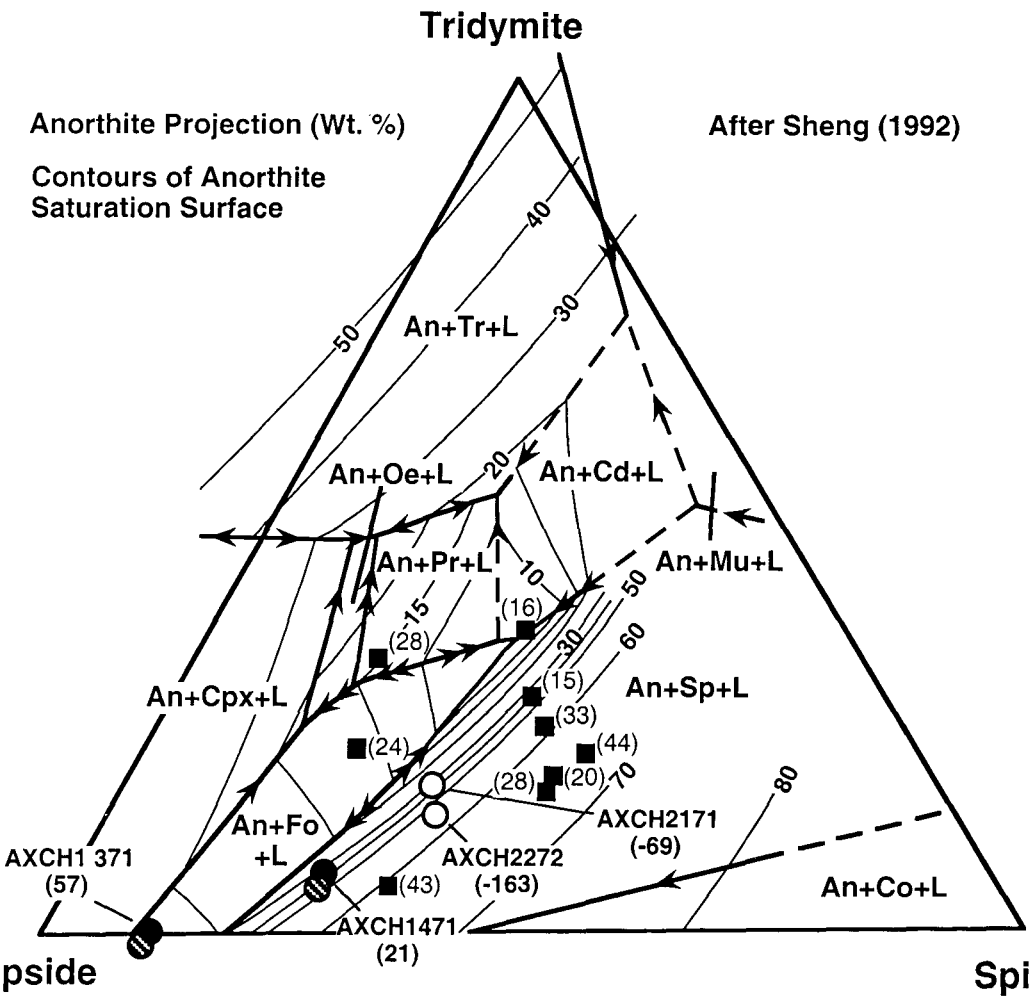

FIG. 14. Ternary diagram of the system diopside–tridymite–spinel projected from anorthite (diagram from Sheng, 1992). Contours give the wt% of anorthite liquid on the anorthite saturation surface. Compositions of the Axtell chondrules are shown along with their An coordinates (see text). Also shown are the Al-rich chondrules from Sheng *et al.* (1991) that have compositions appropriate for this diagram. This diagram is most suitable for investigating the compositions of AXCH-1471 and AXCH-1371. Two projections are plotted for these chondrules. One is the standard projection from anorthite (filled symbols with An coordinates), and the other is projected from both anorthite and albite (hatched symbols). Chondrules AXCH-2171 and AXCH-2272 are shown with open circles but their compositions should not be interpreted from this diagram. Abbreviations: An = anorthite; Tr = tridymite; Cpx = clinopyroxene (diopside); Fo = forsterite; Oe = orthoenstatite; Pr = protoenstatite; Mu = mullite; Sp = spinel; Cd = cordierite; Co = corundum; L = liquid.

The new position is still well above the anorthite saturation surface (Fig. 14) and anorthite remains the predicted liquidus phase.

The barred olivine chondrules, AXCH-2171 and AXCH-2272, are best represented by the diagram diopside–tridymite–spinel projected from forsterite (Fig. 15). Both chondrules project into the Fo + An + L field near to the boundary with the Fo + Sp + L field. Their Fo coordinates place them significantly above the forsterite saturation surface, which is consistent with the textural evidence that forsterite was the liquidus phase. Because the two compositions plot essentially on top of each other, they must lie along a single line connecting forsterite with the projected composition. The two compositions can thus be related to one another by addition or subtraction of olivine.

None of the chondrules has a composition that is multiply saturated, and so it is not possible to demonstrate that igneous differentiation was responsible for any single composition. Chondrules AXCH-1471 and AXCH-1371 do not lie along any predicted fractionation trend, so they are not related by a single igneous differentiation process. In contrast, AXCH-2171 and AXCH-2272 could have formed from a single composition by addition or removal of olivine. Extending the analysis to include POIs from Allende, Adelaide, Leoville, and Vigarano does not improve the picture (see solid squares in Figs. 14 and 15). From the available data, there are no groups of chondrules that are clearly related by a simple igneous fractionation trend. It follows that an origin for Al-rich chondrules from a single Al-rich melt is excluded, but more-complex scenarios cannot be excluded.

Incorporation of Calcium-Aluminum-Rich Inclusion Fragments–A handful of refractory inclusions have been found within chondrules (Bischoff and Keil, 1984; Misawa and Fujita, 1994; Krot *et al.*, 1999; Russell and Kearsley, 1999), which suggests the possibility that assimilation of a CAI by a melt of chondritic material might produce an Al-rich chondrule. To test this hypothesis, we performed two-component mixing calculations using an "unfractionated" endmember and several generic CAI compositions. For the unfractionated, volatile-rich endmember, compositions for CI chondrites and matrices of LL, L, H, and CV chondrites were used (McSween, 1977; Huss *et al.*, 1981; Anders and Grevesse, 1989).

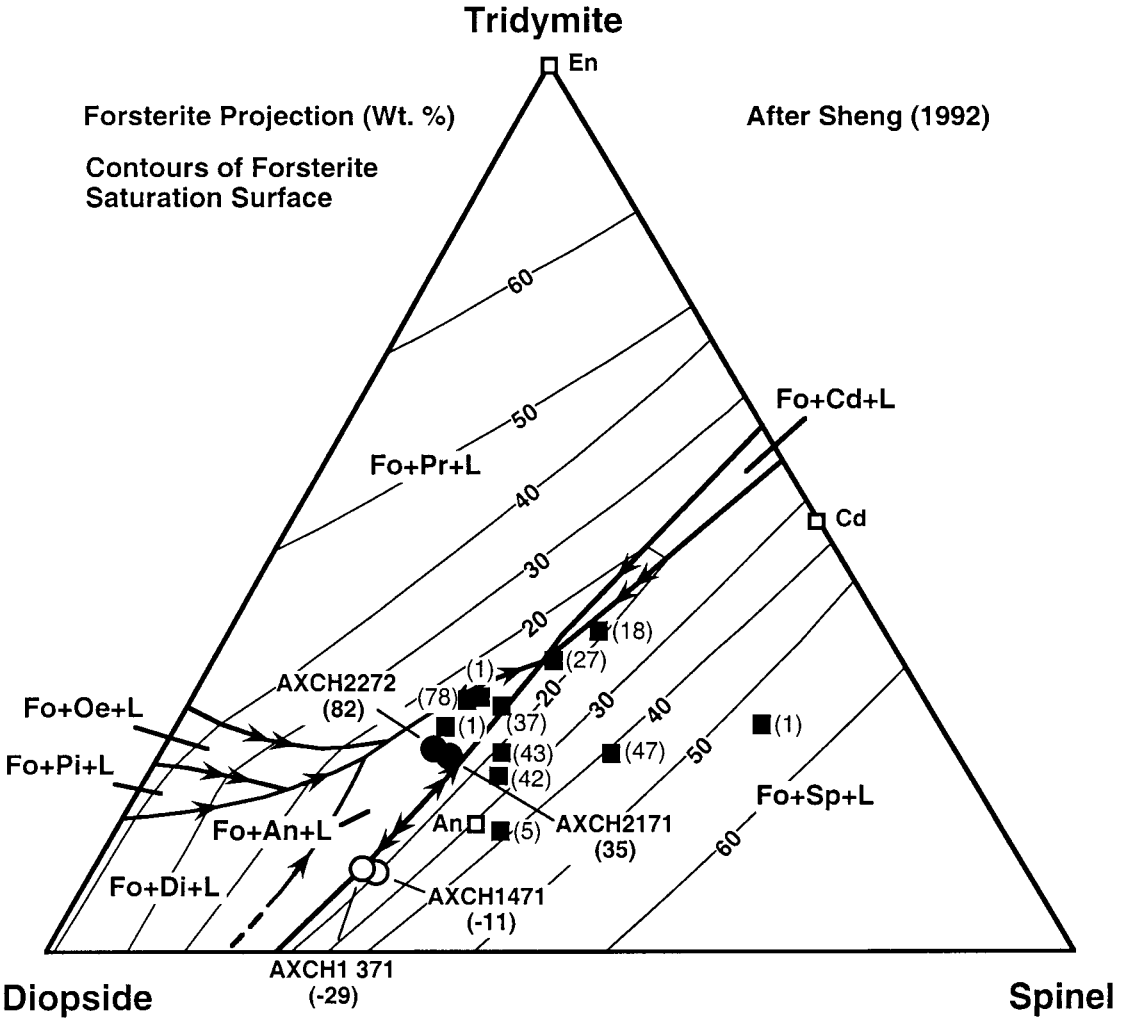

FIG. 15. Ternary diagram of the system diopside–tridymite–spinel projected from forsterite (diagram from Sheng, 1992). Contours give wt% of forsterite liquid on the forsterite saturation surface. Compositions of the Axtell chondrules are shown along with their Fo coordinates. Also shown are the Al-rich chondrules from Sheng *et al.* (1991) that have compositions appropriate for this diagram. This diagram is most suitable for investigating the compositions of AXCH-2171 and AXCH-2272. Chondrules AXCH-1471 and AXCH-1371 are shown with open circles but their compositions should not be interpreted from this diagram. Abbreviations: En = enstatite. Other abbreviations are the same as in Fig. 14.

For the CAI endmember, compositions for compact type-A (Beckett, 1986), fluffy type-A, type-B1, type-B2, and fine-grained inclusions (MacPherson *et al.*, 1988) were used. The calculations assume that CAIs carry a generic enrichment of REEs at ~20 × CI. Ten components (Na_2O, K_2O, MnO, Cr_2O_3, SiO_2, MgO, Al_2O_3, CaO, TiO_2, and Gd for AXCH-1371 and AXCH-2171 or average HREEs for AXCH-1471) were included in the calculation. Iron and Ni were excluded because these elements may be expelled from chondrules as immiscible metal melt droplets during the chondrule-forming melting event (Planner, 1986; Connolly *et al.*, 1994). Calculations were carried out using least-squares regression to determine the proportions of the two components that best match the measured composition (program from M. B. Baker, pers. comm., 1997).

For AXCH-1471, the abundances of Cr_2O_3, SiO_2, MgO, Al_2O_3, CaO, TiO_2, and the heavy REEs are matched to within about ±50% for all combinations of volatile-rich and refractory endmembers. Higher-than-observed abundances of Na_2O, K_2O, and MnO in the calculated compositions can be understood to reflect volatile loss during the chondrule melting event. The minimum value for the sum of the squared residuals was obtained with mixtures of the compact type-A CAI composition with any of the volatile-rich components. The mixture with L3 matrix was marginally better than the others. Mixing proportions (volatile:CAI) were between 0.48:0.52 and 0.54:0.46 and the nonvolatile elements and HREE matched to within ±35%. It is plausible that AXCH-1471 formed *via* assimilation of compact type-A CAI by typical chondritic material during chondrule formation. The low ^{26}Al abundance in AXCH-1471 can be reconciled if assimilation took place considerably after CAIs originally formed.

For AXCH-1371, no combination of our generic CAIs and a volatile-rich composition produced a reasonable match. Calculated Na_2O, K_2O, and MnO abundances are too high, probably because of volatile loss. However, MgO is too high in the calculated compositions by factors of >2, and Cr_2O_3 is too high by factors of ~1.5 to 2.2. Magnesium and Cr should not be lost by volatilization, and common nebular components do not have sufficiently low MgO and Cr_2O_3 to produce a match by mixing with typical CAIs. Thus, it is unlikely that AXCH-1371 formed by assimilation of a common type of CAI into relatively unfractionated material.

For AXCH-2171, all the compositions match to better than a factor of 2 for all components except Na_2O and K_2O. Interestingly, MnO is not depleted to the same extent as the other volatiles. Only a small addition of CAI material is required by the AXCH-2171 composition (mixing proportions (volatile:CAI) are between 0.75:0.25 and 0.82:0.18). The largest mismatches are for MnO, Cr_2O_3, and TiO_2. Because Al_2O_3, CaO, and TiO_2 come primarily from the CAI component, the TiO_2 mismatch would seem to exclude all CAI types except, perhaps, for fluffy or compact type-A. But these two CAI types do not produce a good match for Cr_2O_3. It follows that assimilation of a type-A CAI by normal chondritic material probably does not explain the composition of AXCH-2171. Assimilation of a CAI is also ruled out for AXCH-2272, because its refractory elements are not enriched relative to CI chondrites (Fig. 8b).

The calculations thus show that assimilation of a CAI could explain the compositions of AXCH-1471 but cannot explain the compositions of the other three chondrules.

Evaporation of Average Nebular Material–If evaporation of more volatile components from average nebular material was the process controlling the bulk composition of Al-rich chondrules, the elemental abundances should show a smooth variation as a function of volatility. The abundance pattern need not show complete retention of refractories nor nearly complete loss of volatiles, as predicted by equilibrium calculations, because of kinetic effects.

The abundance pattern for one chondrule, AXCH-1471, roughly matches the pattern expected for evaporation. With the exception of LREEs, all elements more refractory than Sr and Ca are present at ~10 × CI abundances (*e.g.*, Fig. 8a). Relative depletions of other elements generally increase as volatility increases. Iron and Ni contents are considered to be low because of expulsion of immiscible metal melt (Planner, 1986; Connolly *et al.*, 1994). Evaporation of ~90% of SiO_2 and MgO and a loss of 99% of FeO through a combination of evaporation and exclusion of an immiscible metal liquid would produce a ~10× enrichment in the remaining elements. Magnesium is mass fractionated favoring heavy isotopes (F_{Mg} = 2–4‰) but is much less fractionated than would be expected from Rayleigh distillation.

The abundance pattern for AXCH-1371 is not a smooth function of volatility (Fig. 8b). Strontium, Ca, Ti, Al, Sc, Tm, Yb, and Eu are enriched ~10× relative to CI. The remaining REEs, Nb, and Zr are about half as enriched. Iron and Ni are highly depleted. The elemental abundance pattern for this chondrule is not consistent with single-stage evaporation of bulk nebular material. In AXCH-2171, the general enrichment of refractories to 3–5 × CI is consistent with evaporative loss of about half of the SiO_2 and MgO and a loss of 99% of the FeO from a CI composition, but the LREEs are more enriched than the HREEs and Al and Zr are considerably more enriched (Fig. 8c). A single-stage model cannot explain the slight depletions of HREEs relative to LREEs nor can it produce the larger enrichments of Al and Zr. Chondrule AXCH-2271 is not significantly enriched in refractory elements (Fig. 8d).

Although all four chondrules show clear evidence that evaporative loss of volatiles and metal separation played significant roles during chondrule formation, only AXCH-1471 has a bulk composition broadly consistent with single-stage evaporation of bulk chondritic material.

SUMMARY AND CONCLUSIONS

We have carried out a detailed petrochemical study of selected compact type-A and type-B CAIs and plagioclase-bearing chondrules from Axtell ($CV3_{OxA}$). The suite of CAIs and chondrules in Axtell is similar to, but distinct from, that in Allende, another $CV3_{OxA}$ meteorite. Bulk compositional data suggest that CAIs and chondrules are derived from average nebular material, but the mechanisms of formation and the relationships of the different objects are not at all clear. Isotopic evidence indicates that they did not all form in the same isotopic reservoir (Isotopic Results). Petrographic evidence indicate that CAIs and Al-rich chondrules experienced extended histories prior to their incorporation into the meteorite parent bodies. In CAIs, evidence includes irregular and angular shapes, rim sequences that cover the convoluted surfaces and thus postdate the events that shaped the objects, and metasomatism that has altered the primary mineralogy near the surfaces and along cracks. Some of these events are also recorded in the chondrules.

The Al-Mg systematics of chondrules and CAIs place time constraints on this early history. Like in other meteorites, some CAIs in Axtell formed with $(^{26}Al/^{27}Al)_0$ near the canonical value of 5×10^{-5}. Some have remained isotopically undisturbed (Fig. 10b), but others show isotopic evidence of later heating events (Fig. 11). Some inclusions apparently formed with very low $(^{26}Al/^{27}Al)_0$, and some of these have large isotopic anomalies in other elements similar to those of FUN inclusion found in Allende and other meteorites. Aluminum-rich chondrules in Axtell have relatively low $(^{26}Al/^{27}Al)_0$ ranging down from ~3×10^{-6}, like in Allende and other meteorites. The Al-Mg systematics of CAIs and chondrules suggest that formation and alteration of these objects took place over several million years. The presence in a single meteorite of objects with a range of $(^{26}Al/^{27}Al)_0$ and the close proximity of isotopicallly disturbed and undisturbed inclusions imply that CAIs and chondrules formed and were altered over several million years before they accreted into the final meteorite parent bodies.

An extended preaccretionary history is hard to reconcile with the short dynamical lifetimes of chondrule-sized objects because of gas drag in the early solar nebula (*e.g.*, Cameron, 1995). Small objects could survive for extended period in the nebula if they accreted into larger bodies (kilometer-sized?) that are not affected by gas drag. The CAIs and chondrules may have accreted rapidly into relatively large bodies. The high ^{26}Al abundance implied by CAIs would have been a formidable heat source in the earliest of these bodies, probably sufficient to drive metasomatism and thermal metamorphism. Repeated disruptions of these bodies would return CAIs and chondrules from earlier high-temperature events to the nebula where they could be recycled or mixed with the products of later events in later generations of bodies. Meteorites in our collections could be samples of the final stages of this process.

Acknowledgments–We thank J. R. Beckett for useful discussions and M. B. Baker for providing the computer program with which we performed the mixing calculations and advice on its use. We thank E. Jarosewich for permitting us to use his unpublished analysis of Axtell. We also thank T. Ireland and an anonymous reviewer for their constructive reviews. Supported by NASA grant NAG5-4083 (G. J. W.) and NAG5-8158 (G. R. H.). Caltech Division of Geological and Planetary Sciences Contribution #5830 (976).

Editorial handling: S. R. Taylor

REFERENCES

ANDERS E. AND GREVESSE N. (1989) Abundance of the elements: Meteoritic and solar. *Geochim. Cosmochim. Acta* **53**, 197–214.

BECKETT J. R. (1986) The origin of calcium-aluminum-rich inclusions from carbonaceous chondrites: An experimental study. Ph.D. thesis, University of Chicago, Illinois, USA. 373 pp.

BISCHOFF A. AND KEIL K. (1984) Al-rich objects in ordinary chondrites: Related origin of carbonaceous and ordinary chondrites and their constituents. *Geochim. Cosmochim. Acta* **48,** 693–709.

BRIGHAM C. A. (1990) Isotopic heterogeneity in calcium-aluminum-rich meteoritic inclusions. Ph.D. thesis, California Institute of Technology, California, USA. 266 pp.

CAILLET C. AND ZINNER E. K. (1995) The "Porky" inclusion from the Axtell carbonaceous chondrite: A hercynite bearing condensate with large calcium-48 and titanium-50 excesses. *Meteoritics* **30,** 494–495.

CAILLET C., MACPHERSON G. J. AND ZINNER E. K. (1993) Petrologic and Al-Mg isotopic clues to the accretion of two refractory inclusions onto the Leoville parent body: One was hot, the other wasn't. *Geochim. Cosmochim. Acta* **57,** 4725–4743.

CAMERON A. G. W. (1995) The first ten million years in the solar system. *Meteoritics* **30,** 133–161.

CATANZARRO E. J., MURPHY T. J., GARNER E. L. AND SHEILDS W. R. (1966) Absolute isotopic abundance ratios and atomic weight of magnesium. *J. Res. Natl. Bur. Stand.* **70A,** 453–458.

CLARKE R. S., JR., JAROSEWICH E., MASON B., NELEN J., GOMEZ M. AND HYDE J. R. (1970) The Allende, Mexico meteorite shower. *Smithsonian Contrib. Earth Sci.* **5,** 1–55.

CLAYTON R. N., HINTON R. W. AND DAVIS A. M. (1988) Isotopic variations in rock forming elemnts in meteorites. *Phil. Trans. Roy. Soc. London* **A325,** 483–501.

CONNOLLY H. C., JR., HEWINS R. H., ASH R. D., ZANDA B., LOFGREN G. E. AND BOUROT-DENISE M. (1994) Carbon and the formation of reduced chondrules. *Nature* **371,** 136–139.

DAVIS A. M., GROSSMAN L. AND ALLEN J. N. (1978) Major and trace element chemistry of separated fragments from a hibonite-bearing Allende inclusion. *Proc. Lunar Planet. Sci. Conf.* **9th,** 1235–1247.

DAVIS A. M., SIMON S. B. AND GROSSMAN L. (1990) Effective fassaite/liquid trace element distribution coefficients for type B CAI's (abstract). *Lunar Planet. Sci.* **21,** 260–261.

ESAT T. AND TAYLOR S. R. (1984) Correlated REE and Mg anomalies in Allende inclusions (abstract). *Lunar Planet. Sci.* **15,** 252–253.

FAHEY A. J., ZINNER E. K., CROZAZ G. AND KORNACKI A. S. (1987a) Microdistributions of Mg isotopes and REE abundances in a type A calcium-aluminum-rich inclusion from Efremovka. *Geochim. Cosmochim. Acta* **51,** 3215–3229.

FAHEY A. J., GOSWAMI J. N., MCKEEGAN K. D. AND ZINNER E. (1987b) ^{26}Al, ^{244}Pu, ^{50}Ti, REE and trace element abundances in hibonite grains from CM and CV meteorites. *Geochim. Cosmochim. Acta* **51,** 329–350.

GOSWAMI J. N., SRINIVASAN G. AND ULYANOV A. A. (1994) Ion microprobe studies of Efremovka CAIs: I. Magnesium isotope composition. *Geochim. Cosmochim. Acta* **58,** 431–447.

GROSSMAN L. (1975) Petrography and mineral chemistry of Ca-rich inclusions in the Allende meteorite. *Geochim. Cosmochim. Acta* **39,** 433–454.

GROSSMAN L., FRULAND R. M. AND MCKAY D. S. (1975) Scanning electron microscopy of a pink inclusion from the Allende meteorite. *Geophys. Res. Lett.* **2,** 37–40.

GUAN Y., HUSS G. R., MACPHERSON G. J. AND WASSERBURG G. J. (2000) Calcium-aluminum-rich inclusions from enstatite chondrites: Indigenous or foreign? *Science*, **289,** 1330–1333.

HUNEKE J. C., ARMSTRONG J. T. AND WASSERBURG G. J. (1983) FUN with PANURGE: High mass resolution ion microprobe measurements of magnesium in Allende inclusions. *Geochim. Cosmochim. Acta* **47,** 1635–1650.

HUSS G. R., KEIL K. AND TAYLOR G. J. (1981) The matrices of unequilibrated ordinary chondrites: Implications for the origin and history of chondrites. *Geochim. Cosmochim. Acta* **45,** 33–51.

HUSS G. R., MESHIK A. P. AND HOHENBERG C. M. (2000) Abundances of presolar grains in Renazzo and Axtell: Implications for their thermal histories (abstract). *Lunar Planet. Sci.* **31,** #1467, Lunar and Planetary Institute, Houston, Texas, USA (CD-ROM).

HUTCHEON I. D., STEELE I. M., SMITH J. V. AND CLAYTON R. N. (1978) Ion microprobe, electron microprobe and cathodoluminescence data for Allende inclusions with emphasis on plagioclase chemistry. *Proc. Lunar Planet. Sci. Conf.* **9th,** 1345–1368.

HUTCHEON I. D., ARMSTRONG J. T. AND WASSERBURG G. J. (1986) Mg isotopic studies of CAI in CV3 chondrites (abstract). *Lunar Planet. Sci.* **17,** 372–373.

IRELAND T. R., FAHEY A. J. AND ZINNER E. K. (1991) Hibonite-bearing microspherules: A new type of refractory inclusion with large isotopic anomalies. *Geochim. Cosmochim. Acta* **55,** 367–379.

JONES R. H. AND SCOTT E. R. D. (1989) Petrology and thermal history of type 1A chondrules in the Semarkona (LL3.0) chondrite. *Proc. Lunar Planet. Sci. Conf.* **19th,** 523–536.

KROT A. N., SCOTT E. R. D. AND ZOLENSKY M. E. (1995) Mineralogical and chemical modification of components in CV3 chondrites: Nebular or asteroidal processing? *Meteoritics* **30,** 748–775.

KROT A. N., WEBER D., GRESHAKE A, ULYANOV A. A., MCKEEGAN K. D., HUTCHEON I., SAHIJPAL S. AND KEIL K. (1999) Relic Ca,Al-rich inclusions in chondrules from the carbonaceous chondrites Acfer 182 and Acfer 094 (abstract). *Lunar Planet. Sci.* **30,** #1511, Lunar and Planetary Institute, Houston, Texas, USA (CD-ROM).

LATOURRETTE T. AND WASSERBURG G. J. (1998) Mg diffusion in anorthite: Implications for the formation of early solar system planetesimals. *Earth Planet. Sci. Lett.* **158,** 91–108.

LEE T., PAPANASTASSIOU D. AND WASSERBURG G. J. (1976) Demonstration of ^{26}Mg excess in Allende and evidence for ^{26}Al. *Geophys. Res. Lett.* **3,** 109–112.

LEE T., PAPANASTASSIOU D. AND WASSERBURG G. J. (1977) Aluminum-26 in the early solar system: Fossil or fuel? *Astrophys. J.* **211,** L107–L110.

LEE T., RUSSELL W. A. AND WASSERBURG G. J. (1979) Calcium isotopic anomalies and the lack of aluminum-26 in an unusual Allende inclusion. *Astrophys. J.* **228,** L93–L98.

LOSS R. D., LUGMAIR G. W., DAVIS A. M. AND MACPHERSON G. J. (1994) Isotopically distinct reservoirs in the solar nebula: Isotope anomalies in Vigarano meteorite inclusions. *Astrophys. J.* **436,** L193–L196.

MACPHERSON G. J. AND DAVIS A. M. (1993) A petrologic and ion microprobe study of a Vigarano type B refractory inclusion: Evolution by multiple stages of alteration and melting. *Geochim. Cosmochim. Acta* **57,** 231–243.

MACPHERSON G. J. AND HUSS G. R. (2000) Convergent evolution of CAIs and chondrules: Evidence from bulk compositions and a cosmochemical phase diagram (abstract). *Lunar Planet. Sci* **31,** #1796, Lunar and Planetary Institute, Houston, Texas, USA (CD-ROM).

MACPHERSON G. J., WARK D. A. AND ARMSTRONG J. T. (1988) Primitive material surviving in chondrites. In *Meteorites and the Early Solar System* (eds. J. F. Kerridge and M. S. Mathews), pp. 746–807. Univ. Arizona Press, Tucson, Arizona, USA.

MACPHERSON G. J., DAVIS A. M. AND ZINNER E. K. (1995) The distribution of aluminum-26 in the early Solar System—A reappraisal. *Meteoritics* **30,** 365–386.

MAO X-Y., WARD B. J., GROSSMAN L. AND MACPHERSON G. J. (1990) Chemical compositions of refractory inclusions from Vigarano and Leoville carbonaceous chondrites. *Geochim. Cosmochim. Acta* **54,** 2121–2132.

MASON B. AND MARTIN P. M. (1977) Geochemical differences among components of the Allende meteorite. *Smithsonian Contrib. Earth Sci.* **19,** 84–95.

MASON B. AND TAYLOR S. R. (1982) Inclusions in the Allende meteorite. *Smithsonian Contrib. Earth Sci.* **25,** 30 pp.

MCKEEGAN K. D., GREENWOOD J. P., LESHIN L. AND COSARINSKY M. (2000) Abundance of ^{26}Al in ferromagnesian chondrules of unequilibrated ordinary chondrites (abstract). *Lunar Planet. Sci.* **31,** #2009, Lunar and Planetary Institute, Houston, Texas, USA (CD-ROM).

MCSWEEN H. Y., JR. (1977) Petrographic variations among carbonaceous chondrites of the Vigarano type. *Geochim. Cosmochim. Acta* **41,** 1777–1790.

MISAWA K. AND FUJITA T. (1994) A relict refractory inclusion in a ferromagnesian chondrule from the Allende meteorite. *Nature* **368,** 723–726.

MOUSTEFAUOI S., KITA N., NAGAHARA H., TOGASHI S. AND MORISHITA Y. (1999) Aluminum-26 in two ferromagnesian chondrules from a highly unequilibrated ordinary chondrite: Evidence of a short period of chondrule formation (abstract). *Meteorit. Planet. Sci.* **34 (Suppl.),** A84.

NIEDERER F. R., PAPANASTASSIOU D. A. AND WASSERBURG G. J. (1981) The isotopic composition of titanium in the Allende and Leoville meteorites. *Geochim. Cosmochim. Acta* **45,** 1017–1031.

PLANNER H. N. (1986) Appearance of metal at the chondrule surface during chondrule melting. *Meteoritics* **21,** 484–485.

PODOSEK F. A., ZINNER E. K., MACPHERSON G. J., LUNDBERG L. L., BRANNON J. C. AND FAHEY A. J. (1991) Correlated study of initial ^{87}Sr/^{86}Sr and Al/Mg systematics and petrologic properties in a suite of refractory inclusions from the Allende meteorite. *Geochim. Cosmochim. Acta* **55,** 1083–1110.

RUSSELL S. S. AND KEARSLEY A. (1999) Relict refractory inclusions within chondrules from CV meteorites (abstract). *Meteorit. Planet. Sci.* **34 (Suppl.),** A99–A100.

RUSSELL S. S., SRINIVASAN G., HUSS G. R., WASSERBURG G. J. AND MACPHERSON G. J. (1996) Evidence for widespread ^{26}Al in the solar nebula and new constraints for nebula time scales. *Science* **273,** 757–762.

RUSSELL S. S., HUSS G. R., FAHEY A. J., GREENWOOD R. C., HUTCHISON R. AND WASSERBURG G. J. (1998) An isotopic and petrologic study of

calcium-aluminum-rich inclusions from CO3 meteorites. *Geochim. Cosmochim. Acta* **62,** 689–714.

RUSSELL W. A., PAPANASTASSIOU D. A. AND TOMBRELLO T. A. (1978) Ca isotope fractionation on the Earth and other solar solar system materials. *Geochim. Cosmochim. Acta* **42,** 1075–1090.

SHENG Y. J. (1992) The origin of plagioclase olivine inclusions. Ph.D. thesis, California Institute of Technology, California, USA. 271 pp.

SHENG Y. J., HUTCHEON I. D. AND WASSERBURG G. J. (1991) Origin of plagioclase-olivine inclusions in carbonaceous chondrites. *Geochim. Cosmochim. Acta* **55,** 581–599.

SIMON S. B., GROSSMAN L. AND WACKER J. F. (1994) Unusual refractory inclusions from a CV3 chondrite found near Axtell, Texas (abstract). *Lunar Planet. Sci.* **25,** 1275–1276.

SIMON S. B., GROSSMAN L., CASANOVA I., SYMES S., BENOIT P., SEARS D. W. G. AND WACKER J. F. (1995) Axtell, a new CV3 chondrite find from Texas. *Meteoritics* **30,** 42–46.

SRINIVASAN G., HUSS G. R. AND WASSERBURG G. J. (1996) Aluminum-26 time scales and processes connecting plagioclase-rich chondrules and CAIs (abstract). *Meteorit. Planet. Sci.* **31 (Suppl.),** A133.

SRINIVASAN G., HUSS G. R. AND WASSERBURG G. J. (1997) Precursors of aluminum-rich chondrules from the Axtell (CV3) meteorite. *Meteorit. Planet. Sci.* **32 (Suppl.),** A123–A124.

STEGMANN W. AND BEGEMANN F. (1981) Al-correlated ^{26}Mg excesses in a large Ca-Al-rich inclusion of the Leoville meteorite. *Earth Planet. Sci. Lett.* **55,** 266–272.

STOLPER E. (1982) Crystallization sequences of Ca-Al-rich inclusions from Allende: An experimental study. *Geochim. Cosmochim. Acta* **46,** 2159–2180.

SYLVESTER P. J., GROSSMAN L. AND MACPHERSON G. J. (1992) Refractory inclusions with unusual chemical compositions from the Vigarano carbonaceous chondrite. *Geochim. Cosmochim. Acta* **56,** 1343–1363.

WARK D. A. AND LOVERING J. F. (1977) Marker events in the early evolution of the solar system: Evidence from rims on Ca-Al-rich inclusions in carbonaceous chondrites. *Proc. Lunar. Sci. Conf.* **8th,** 95–112.

WARK D. A. AND LOVERING J. F. (1982) The nature and origin of type B1 and type B2 Ca-Al-rich inclusions in the Allende meteorite. *Geochim. Cosmochim. Acta* **46,** 2581–2594.

WASSERBURG G. J. AND PAPANASTASSIOU D. A. (1982) Some short-lived nuclides in the early solar system—A connection with the placental ISM. In *Essays in Nuclear Astrophysics* (eds. C. A. Barnes, D. D. Clayton, D. W. Schramm and W. A. Fowler), pp. 77–140. Cambridge Univ. Press, New York, New York, USA.

WASSERBURG G. J., LEE T. AND PAPANASTASSIOU D. A. (1977) Correlated O and Mg isotopic anomalies in Allende inclusions: II. Magnesium. *Geophys. Res. Lett.* **4,** 299–302.

WEISBERG M. K., PRINZ M., CLAYTON R. N. AND MAYEDA T. K. (1997) CV3 chondrites: Three subgroups, not two (abstract). *Meteorit. Planet. Sci.* **31 (Suppl.),** A138–A139.

WOOD J. (1996) Why did some CAIs contain ^{26}Al and others not? (abstract). *Meteorit. Planet. Sci.* **31 (Suppl.),** A154–A155.

ZINNER E. K. AND CROZAZ G. (1986) A method for the quantitative measurement of rare earth elements in the ion microprobe. *Int. J. Mass Spect. Ion Proc.* **69,** 17–38.